

Near-Infrared Variability Study of the Central $2.3' \times 2.3'$ of the Galactic Centre II. Identification of RR Lyrae Stars in the Milky Way Nuclear Star Cluster

Hui Dong¹, Rainer Schödel¹, Benjamin F. Williams², Francisco Noguerras-Lara¹, Eulalia Gallego-Cano¹, Teresa Gallego-Calvente¹, Q. Daniel Wang³, R. Michael Rich⁴, Mark R. Morris⁴, Tuan Do⁴, Andrea Ghez⁴

¹ *Instituto de Astrofísica de Andalucía (CSIC), Glorieta de la Astronomía S/N, E-18008 Granada, Spain*

² *Department of Astronomy, Box 351580, University of Washington, Seattle, WA 98195, USA*

³ *Department of Astronomy, University of Massachusetts, Amherst, MA, 01003, USA*

⁴ *Department of Physics and Astronomy, University of California, Los Angeles, CA, 90095, USA*

ABSTRACT

Because of strong and spatially highly variable interstellar extinction and extreme source crowding, the faint ($K \geq 15$) stellar population in the Milky Way's nuclear cluster is still poorly studied. RR Lyrae stars provide us with a tool to estimate the mass of the oldest, relative dim stellar population. Recently, we analyzed *HST*/WFC3/IR observations of the central $2.3' \times 2.3'$ of the Milky Way and found 21 variable stars with periods between 0.2 and 1d. Here, we present a further comprehensive analysis of these stars. The period-luminosity relationship of RR Lyrae is used to derive their extinctions and distances. Using multiple approaches, we classify our sample as four RRc, four RRab and three candidates, ten binaries. Especially, the four RRabs show sawtooth light curves and fall exactly onto the Oosterhoff I division in the Bailey diagram. Compared to the RRabs reported by Minniti et al, 2016, our new RRabs have higher extinction ($A_K > 1.8$) and should be closer to the Galactic Centre. The extinction and distance of one RRab match those for the nuclear star cluster given in previous works. We perform simulations and find that after correcting for incompleteness, there could be no more than 40 RRabs within the nuclear star cluster and in our field-of-view. Through comparing with the known globular clusters of the Milky

Way, we estimate that if there exists an old, metal-poor ($-1.5 < [\text{Fe}/\text{H}] < -1$) stellar population in the Milky Way nuclear star cluster on a scale of $5 \times 5 \text{ pc}$, then it contributes at most $4.7 \times 10^5 M_{\odot}$, i.e., $\sim 18\%$ of the stellar mass.

Keywords: infrared: stars < Resolved and unresolved sources as a function of wavelength, stars: variables: RR Lyrae < Stars, Galaxy: centre < The Galaxy

1. Introduction

Nuclear star clusters (NSCs) have been discovered in 60-70% of all types of local galaxies. NSCs typically have sizes similar to globular clusters, but are 1-2 orders of magnitude brighter. Thus, they are the most massive and dense stellar systems in the present-day Universe. The masses of NSCs are correlated with the masses of their host galaxies. NSCs, normally characterized by complex stellar populations, often show signs of recurrent and very recent star formation (see Böker et al. 2002, 2004; Walcher et al. 2005, 2006; Carson et al. 2015; Georgiev et al. 2016, and references therein).

Two mechanisms have been proposed for the formation of NSCs: (1) NSCs could grow largely *in-situ* through gas infall followed by star formation or by accretion of clusters formed in their close environment (Agarwal & Milosavljević 2011; Neumayer et al. 2011; Bekki et al. 2006). These scenarios are supported by, among other forms of evidence, the flattening and rotation observed in NSCs of edge-on galaxies and by the presence of young ($\leq 100 \text{ Myr}$) stellar populations in some NSCs (Walcher et al. 2006). In particular, *in-situ* star formation occurred a few Myr ago in the centre of the Milky Way and may still be ongoing (Genzel et al. 2010; Lu et al. 2013; Yusef-Zadeh et al. 2015, and references therein). (2) NSCs may also have acquired a significant fraction of their masses through the infall and dissolution of globular clusters due to dynamical friction and tidal forces (e.g. Tremaine et al. 1975; Lotz et al. 2001; Antonini et al. 2012). Globular clusters could thus have contributed to the population of the oldest stars. Around 5% of the stars in the NSC have been found to have $[\text{Fe}/\text{H}] \leq -0.5$ and may have been contributed by old metal-poor globular clusters (Do et al. 2015; Feldmeier-Krause et al. 2017; Schultheis et al. 2016; Ryde & Schultheis 2015, Rich et al. 2017, in preparation). It is also possible that both *in-situ* star formation and globular cluster infall may have contributed to the growth of NSCs (e.g. Hartmann et al. 2011). Detailed stellar population studies of NSCs are required to assess the relative importance of these two scenarios.

The large distances to extragalactic nuclei limit us to the study of only their integrated light, which is averaged over scales between a parsec and tens of parsecs, is dominated by

the brightest stars, and may even be contaminated by nuclear activity. In contrast, the GC is located only ~ 8 kpc from us (Ghez et al. 2008; Gillessen et al. 2009; Boehle et al. 2016), or about a hundred times closer than the second nearest, comparable NSC in the Andromeda galaxy. Because of this proximity, the GC is the only nucleus where we can conduct spatially resolved population studies (e.g., Schödel et al. 2009; Buchholz et al. 2009; Genzel et al. 2010).

The Milky Way’s NSC (MWNSC hereafter) has a half-light radius of approximately 4 pc and a total mass of roughly $2.5 \times 10^7 M_\odot$ (Schödel et al. 2014; Fritz et al. 2016). The cluster’s rotation axis is parallel to that of the Galactic Disk (Feldmeier et al. 2014; Fritz et al. 2016). The cluster is also known to have a quasi-continuous, complex star formation history (see Pfuhl et al. 2011, and references therein). The most recent burst of star formation in the MWNSC happened ~ 3 -6 Myr ago (e.g., Paumard et al. 2006; Lu et al. 2013). The combination of MWNSC, large Nuclear Stellar Disk and Nuclear Molecular Disk is called the Nuclear Bulge, which, in projection, appears to be a flat bar with an outer radius of 230 pc and a scale height of 45 pc (Launhardt et al. 2002).

While the most recently formed stars are generally believed to have formed *in situ* (see, e.g., discussions in Genzel et al. 2010 or Lu et al. 2013), there is still no compelling evidence for the presence of a stellar population that may have been contributed by globular cluster infall. As a first step, finding such evidence requires identifying ~ 10 Gyr old stars. Subsequently, one could study the distribution and dynamics of such a population to see whether it can result from the infall scenario. Because of the extreme interstellar extinction and strong source crowding toward the GC, current imaging studies with adaptive optics (AO) assisted 8m-class telescopes can achieve only a $\sim 50\%$ completeness limit of $K_s \approx 18.5$ (Schödel et al. 2014b, 2017; Gallego-Cano et al. 2017). Spectroscopic studies are generally limited to $K_s \leq 16$ (Pfuhl et al. 2011). The mean mass of the spectroscopically accessible, $K_s = 15 - 16$ Red Clump (RC) giants is $> 1 M_\odot$ (see Fig. 16 in Schödel et al. 2007), which means that they may not be old enough to serve as potential tracers of ancient globular cluster infall.

RR Lyrae (RRL) stars provide us with a method to study the old stellar populations (> 10 Gyr old, Walker 1989; Lee 1992; Pietrukowicz et al. 2016). RRL stars are low-mass core-helium-burning stars with oscillation amplitudes in the $0.1 < \delta K_s < 0.5$ mag range and period range between about 0.2 and 1 d. Although there are metal-rich RRLs observed in the Galactic Disk (see Chadid et al. 2016, and references therein), the majority of RRLs are found in metal-poor globular clusters (Catelan 2009). Based on the amplitude-period diagram of such RRLs (also known as a Bailey diagram), the globular clusters in the Milky Way can be divided into two types: Oosterhoff type I and II (OoI and OoII, hereafter).

In general, the OoI clusters ($[\text{Fe}/\text{H}] \sim [-1.0, -1.5]$) seem to be more metal-rich than the OoII clusters ($[\text{Fe}/\text{H}] \sim [-1.5, -2.5]$) (Fig. 5 in Catelan 2009). Therefore, by finding RRL stars and determining their distribution between these two types, we can provide new constraints on the formation history of the MWNSC.

RRL stars can be classified into three groups: Fundamental-mode RRLs (Type ab, RRab hereafter), first-overtone RRLs (type c, RRC hereafter), and the rare double-mode RRLs (type d). The light curve of an RRab star is very unique, with a broad maximum, a sharp minimum, and a steep ascending branch. In contrast, the light curve of an RRC star is typically rather symmetric and can be fitted with a single sine function. Also, the periods of RRab stars are longer than those of RRC stars; they can be distinguished at a period of 0.4 d (Gran et al. 2015).

The biggest challenge to detecting RRL stars in the MWNSC is their intrinsic faintness. Accounting for the appropriate extinction and distance modulus of the GC, their observed magnitudes are $K \approx 17$ mag and $H \approx 18.5$ mag, below the detection threshold of the seeing-limited (FWHM $\approx 0.7''$) VISTA Variables in the Via Lactea Survey (VVV) that consists of multi-epoch near-infrared (near-IR) imaging observations of the Galactic Bulge and southern Disk since 2010 (Minniti et al. 2010). Although Minniti et al. (2016) recently reported the detection of RRL stars in the Galactic Nuclear Bulge, the locations and relatively low extinctions of these stars suggest that they are in the foreground of the Galactic Bulge (see discussion in §4.1).

We follow up here on our recent analysis of the Hubble Space Telescope (*HST*) Wide Field Camera 3 (WFC3) IR observations covering the central $2.3' \times 2.3'$ ($\sim 5 \times 5$ pc²) of the MWNSC. Thanks to the high angular resolution ($\sim 0.2''$), sensitivity, and stability of these observations we have identified 3894 variable sources (Dong et al. 2017, Paper I) and have further derived the periods for 36 of these sources. The periods, as well as observed magnitudes and colours of several of the sources, indicate that they are RRL candidates probably located in the Nuclear Bulge or even in the MWNSC.

The rest of this paper is organized as follows. We briefly describe our observations, data analysis, and steps to calculate the extinction and distance using the near-IR period-luminosity (PL) relationship of our RRL candidates in §2. We classify the types of candidates on the basis of their periods/magnitudes/colors and estimate the contamination from eclipsing binaries in §3. In §4, we discuss the relationship of our identified RRL stars to the Nuclear Bulge and the MWNSC and explore the limits that the detection of these stars places on the oldest stellar population in the GC and on the globular cluster infall scenario. We summarize our results in §5.

2. Observations, data reduction and analysis

2.1. *HST* dataset and variable source catalog

Observations, data reduction, and identification of variable sources have already been described in Paper I. Here, we only briefly summarize the key points.

The *HST*/WFC3 IR observations in the F127M (1.27 μm) and F153M (1.53 μm) bands that we used were from programs GO-11671, GO-12318, GO-12667, GO-12182, GO-13049, GO-13116, and GO-13403 (Hosek et al. 2015; Støstad et al. 2015; Mossoux et al. 2016). In terms of their effective wavelengths, F127M and F153M are the analogs of the Johnson-Glass J band (1.22 μm) and H band (1.63 μm) filters. The observations in the F153M band, acquired between 2010 and 2014, include 290 dithered exposures, ranging from 250 to 350 seconds each. The total length of the exposures in the first three years is less than 6 hours, but the observation blocks in 2014 are long: 10 hours on Feb 28, 10 hours on Mar 10, 15 hours on April 2, and 5.5 hours on April 3. These blocks are critical in our identification of RRL stars, because of the significant coverage of their periods. We use the observations in the F127M band to determine F127M-F153M colours of the stars, which helps to locate them in the foreground/background or in the MWNSC proper. The total duration of the F127M observations is less than 2 hours. Therefore, they can only cover a small fraction of the periods of the RRL stars.

We used ‘DOLPHOT’ (Dolphin 2000) to detect sources, extract photometry from individual dithered exposures, and empirically determine the photometric variations among exposures. We further used the least χ^2 method to identify variable stars and then the Lomb-Scargle periodogram analysis (Lomb 1976; Scargle 1982) to calculate the periods of 36 sources with well-covered light curves within the individual observation blocks in 2014. We found that 21 sources have periods between 0.2 and 1 d, and therefore could be RRL stars. Table 1 lists their IDs in Dong et al. (2017, Paper I), celestial coordinates, periods, as well as F127M and F153M magnitudes and the corresponding uncertainties. To simplify the presentation in this paper, we label RRL candidates as R1 to R21.

Fig 1 shows a mosaic image from the *HST*/WFC3 IR F153M observations overlaid with the positions of the 21 sources and Fig. 2 gives their finding charts. Fig. 3 presents the colour magnitude diagram (CMD, F127M-F153M vs. F153M) of detected sources within $2''$ of each RRL candidate. The folded light curves are shown in Fig. 4.

2.2. Fourier fitting of folded light curves

We used the direct Fourier fitting (DFF) method given in Kovács & Kupi (2007) to analyze the folded light curves of these 21 variable stars. This method fit the data with the following equation:

$$F153M(\phi) = A_0 + \sum_{i=1}^N A_i \sin(2\pi i\phi + \Phi_i) \quad (1)$$

where ϕ is the phase of the individual observation, and Φ is the reference phase, and N is the maximum order, which is always ≤ 6 to prevent over-fitting the light curves. The definition of the Fourier coefficients in Table 2 are given below

$$A_{i1} = \frac{A_i}{A_1} \quad (2)$$

$$\Phi_{i1} = \Phi_i - i\Phi_1 \quad (3)$$

The routine also outputs the $\langle F153M \rangle$ (A_0), the mean F153M magnitude. From the fitting parameters, we also derived the peak-to-peak amplitude, i.e., the difference between the maximum and the minimum magnitudes.

2.3. Extinctions and distances

We derived foreground extinctions and distances of the RRL candidates from their apparent F127M/F153M magnitudes, with the help of the PL relationship of RRL stars.

Since the observations in the F127M and F153M bands probably cover different phases of the light curves, the observed F127M-F153M colours are biased. For each star, we calculated first its average F127M magnitude, $\langle F127M \rangle$ and then its colour $\langle F127M \rangle - \langle F153M \rangle$. We estimated $\langle F127M \rangle$ using the F127M magnitude from the observations of Program GO-11671, and, if unavailable, Program GO-12182. The estimate assumed that the light curves in the F127M band are similar to those in the F153M band, but may have different amplitudes, used Equations (B3) and (B4) in Feast et al. (2008)¹:

$$\Delta F127M = -0.015 + 2.18447 \times (\Delta F153M - 0.111) \quad (4)$$

This procedure introduces a ~ 0.1 mag systematic uncertainty into the $F127M$ magnitude according to Feast et al. (2008) and Gran et al. (2015). From the artificial $F127M$ light curves

¹Feast et al. (2008) use J and H in their Equations (B3) and (B4). Considering the closeness of the effective wavelengths between J/H and F127M/F153M (§2.1), we assume $\Delta F127M = \Delta J$ and $\Delta F153M = \Delta H$.

and the phases of the F127M observations, we then calculated the difference between the observed $F127M$ magnitude and $\langle F127M \rangle$, which could be up to 0.27 mag. The diamonds and crosses in Fig. 5 represent the colors, $F127M - \langle F153M \rangle$ (diamonds) and $\langle F127M \rangle - \langle F153M \rangle$ (pluses). Most of the candidates, have $\langle F127M \rangle - \langle F153M \rangle > 1.5$, except for R1 ($\langle F127M \rangle - \langle F153M \rangle = 0.58$), which we therefore conclude is a foreground object.

Subsequently, we derived the absolute magnitudes (M_{F127M} and M_{F153M}) of our RRL candidates. Unlike in the ultraviolet and optical bands, the PL relation for RRL stars in the near-IR is tight (Longmore et al. 1990) and is not sensitive to metallicity. Catelan et al. (2004) give the following dependence:

$$M_J = -0.141 - 1.773 \times \log P + 0.190 \times \log Z \quad (5)$$

$$M_H = -0.551 - 2.313 \times \log P + 0.178 \times \log Z \quad (6)$$

where P and Z are the period and metallicity, while M_J and M_H are the absolute magnitudes in the Johnson-Cousins-Glass system. Catelan et al. (2004) give the following conversion between Z and $[\text{Fe}/\text{H}]$: $\log Z = [\text{Fe}/\text{H}] - 1.765$, with the assumption that the solar metallicity is 0.01716. In Appendix A, we derive conversions from M_J and M_H to $F127M$ and $F153M$ for RRL stars, with uncertainties of only 0.003 mag and 0.006 mag, respectively. In principle, the metallicity of RRL stars can be estimated from their periods and phases (such as Φ_{31} ; Jurcsik & Kovacs 1996; Smolec 2005). Unfortunately, the empirical relationship for such estimation is available only in the V and I bands. Therefore, we adopted values $\langle [Fe/H] \rangle = -1.02$ with a dispersion of 0.25 dex from Pietrukowicz et al. (2012), who studied $\sim 17,000$ RRL stars in the Galactic Bulge from the OGLE survey. A similar value, $\langle [Fe/H] \rangle = -1.0$ with a dispersion of 0.16 dex, is reported by Walker & Terndrup (1991) for RRLs in Baade's window ($l=1.0317$, $b=-03.9097$), not far from the GC, but with substantially lower foreground extinction. The derived M_{F127M} and M_{F153M} are given in Table 3. The uncertainties of M_{F127M} and M_{F153M} , which are also included in Table 3, account for both the uncertainty of the metallicity (0.25 dex) and that of the conversions from M_J and M_H to $F127M$ and $F153M$ given above.

Next, we calculated the interstellar extinction A_K from the observed magnitudes and the absolute magnitudes:

$$A_K = \frac{(\langle m_{F127M} \rangle - \langle m_{F153M} \rangle) - (M_{F127M} - M_{F153M})}{\frac{A_{F127M}}{A_K} - \frac{A_{F153M}}{A_K}} \quad (7)$$

where $\frac{A_{F127M}}{A_K}$ and $\frac{A_{F153M}}{A_K}$ are the relative extinctions, determined by the extinction law, $A_\lambda \propto \lambda^\alpha$ (Draine 1989). Appendix B gives the method to translate different α to $\frac{A_{F127M}}{A_K}$ and $\frac{A_{F153M}}{A_K}$ for the RRL stars. This step could introduce the largest systematic uncertainty

into our analysis. For example, Dékány et al. (2015) and Matsunaga et al. (2016) show that the different values of α given in the literature can result in systematic uncertainties of 0.2-0.4 mag in the calculated distance modulus of Classical Cepheids in the inner part of the Galaxy. The α towards the GC is known to be different from that of the solar neighborhood (-1.75, Draine 1989), but its exact value is still uncertain. For example, while Nishiyama et al. (2006) find $\alpha = -1.99 \pm 0.02$, Gosling et al. (2009) claim that α varies from one line-of-sight to another, with a mean value and standard deviation of -2.64 ± 0.52 . The two most relevant works on α related to the MWNSC are Fritz et al. (2011) and Schödel et al. (2010), because they analyze specifically the extinction curves toward the central parsec of the Milky Way. Fritz et al. (2011) use hydrogen emission lines to derive $\alpha = -2.11 \pm 0.06$ and $A_{2.166} = -2.62 \pm 0.11$ in the inner $14'' \times 20''$. Schödel et al. (2010) use the RC stars detected within the central $40'' \times 40''$ to obtain $\alpha = -2.21 \pm 0.24$ and $A_K = 2.54 \pm 0.12$. These results agree well within the uncertainties. For our analysis here, we use three different values of $\alpha = -2.0, -2.1, -2.2$ to obtain A_{K_s} values of the RRL candidates (Table 3). The less negative α is, the larger is A_{K_s} . Nevertheless, A_{K_s} values obtained from assuming $\alpha = -2.1$ overlap with those obtained from the other two values within their uncertainties.

Finally, we estimate the distance moduli (DM) of the RRL stars from the following equations:

$$DM = \langle F_{153M} \rangle - M_{F_{153M}} - A_{F_{153M}} \quad (8)$$

$$= \langle F_{153M} \rangle - M_{F_{153M}} - \frac{A_{F_{153M}}}{A_K} A_K \quad (9)$$

From the DM, we then infer the distances, as well as their uncertainties (Table 3).

3. Classification

Based on these properties of the variables, we make classifications of them, in particular, separating between W UMa and RRL candidates. W UMa stars are eclipsing low-mass overcontact binaries and have periods between 0.2 to 1 d, in the same range as RRL stars. They are intrinsically less luminous than RRL stars. Like RRc stars, their light curves are sine-shaped. Meanwhile, the light curves of RRab stars could be more sinusoidal in the near-IR and have a significantly lower amplitude than in the visible regime (Catelan et al. 2013). Therefore, the shape of the observed light curves by themselves may in some cases not be sufficient to distinguish between RRab stars with sinusoidal light curves (RRab?, hereafter) and W UMa binaries. In the following, we will therefore use three steps to distinguish between RRab, RRc and W UMa binaries.

3.1. Periods and light curves

Of our 21 sources, 8 have periods shorter than 0.4 d and are thus possibly RRc candidates. The remaining 13 could be of type RRab. Especially, in the latter group, R3, R5, R15 and R16 show very typical asymmetric RRab light curves (see Fig. 4). Instead, the light curve of R4 increases too slowly from the minimum to the maximum, which is somewhat unusual for a RRab star. The folded light curves of R19 and R20 are too noisy for a reliable classification. The other light curves are symmetric (sinusoidal), which makes it difficult to decide whether they are RRL stars or eclipsing binaries.

3.2. Extinction

Comparing the extinctions derived in §2.3 with an extinction map derived from the RC stars provides us with another tool to distinguish between W UMa and RRL stars. The intrinsic luminosity – and thus also the distance – of potential W UMa stars would have been overestimated by our use of the PL relationship of RL stars in §2.3. Nogueras-Lara et al. (in preparation) use the RC stars detected in *JHK VLT/HAWK-I* observations of a field of about $7.5' \times 3'$ centered on Sgr A* to construct an extinction map with an angular resolution of $\sim 2''$, assuming $\alpha = -2.2$. If our sample stars are foreground (background) RRL stars in the Galactic Bulge with distances smaller (larger) than the GC distance of 7.86 ± 0.18 kpc (Boehle et al. 2016, see also Gillessen et al. 2016), the extinctions derived in §2.3 should be significantly smaller (larger) than the values of this extinction map at their corresponding locations. These extinction values are also listed in Table 3.

A plot of the differences between the extinction values estimated in §2.3 and those from the extinction map of Nogueras-Lara et al. (in preparation) plotted over the calculated distances in §2.3 is shown in Fig 6. The calculated extinction values of all our sample are smaller than those from the extinction map. This is because 1) stars in front of the GC with higher extinction than those from the extinction map are not expected and 2) the dense molecular clouds in the circumnuclear ring (Lau et al. 2013, and references therein) dim background RRL stars and W UMa binaries, which causes them to be undetected or be unclassified as variable stars due to larger photometric uncertainties.

All stars in our field behind the GC have to suffer at least the interstellar extinction toward the GC. It is unphysical for a star to lie at a greater distance while at the same time suffer a lower interstellar extinction, in particular, because we can reasonably assume the presence of interstellar dust on the far side of the GC, too. We therefore assume that stars that show this discrepancy are W UMa binaries misclassified as RRLs. We therefore classify

eight stars (R1, R4, R10, R12, R17, R18, R20, R21) with distances derived in §2.3 with $\alpha=-2.2$ larger than 8 kpc by more than three times the corresponding distance uncertainties as potential eclipsing binaries. Fig. 3 shows that their $F127M-F153M$ colours are similar or bluer than the majority of nearby sources, which should be within the Galactic Nuclear Bulge, and are inconsistent with the possibility that they are background RRLs.

3.3. Bailey diagram

Fig. 7 is the K_s band Bailey diagram for our sources along with the data for a reference sample of RRab (Gran et al. 2016) and RRC stars (Gran et al. 2015), derived from the VVV survey. Equations (B4) and (B5) in Feast et al. (2008) show how to translate the F153M amplitudes into the Ks -band for the RRL stars.

$$\Delta K_s = 0.176 + 0.606796 \times (\Delta F153M - 0.111) \quad (10)$$

We can see that 1) the RRC and RRab stars from our sample lie perfectly within the range for these RRL stars from the VVV survey. Especially, the seven RRab stars and candidates are located very close to the OoI line. 2) Probable W UMa binaries as identified in §3.2 are widely distributed throughout the Bailey diagram. 3) Finally, two stars, R6 and R14 (open boxes), are located near the edge of the cloud of RRab stars. Therefore, they may be RRabs or eclipsing candidates.

To summarise, our 21 sources include four RRC stars, four RRab stars, three RRab?s, as well as ten probable eclipsing binaries.

4. Discussion

Here, we discuss the physical relationship between RRL stars in our sample and the MWNSC, estimate the total number of RRab stars in the MWNSC and constrain the fraction of the old stellar population.

4.1. Physical locations of the detected RRL stars

In order to obtain constraints on the old stellar population in the MWNSC, we need to identify which of our identified RRL stars are part of the MWNSC. We first use the extinctions and distances determined in §2.3 to constrain the line-of-sight locations of our RRL stars with respect to the MWNSC.

Within our sample, three RRL stars lie close to Sgr A* along the line of sight within less than the distance uncertainties derived in §2.3 and have $A_K > 2$: R13, R15 and R19, according to their distances with $\alpha = -2.2$ (see Table 3). The A_K values of R13 and R15 are smaller than the corresponding values from the extinction map of Nogueras-Lara et al. (in preparation), by at least five sigma, while the A_K of R19 is consistent with the extinction map within two sigma. On the other hand, the $F127M-F153M$ colours of these stars are similar to those of the majority of nearby sources in Fig. 3. Therefore, as suggested by their distance, R13 and R19 could be naturally explained by an RRc star and an RRab? in the foreground and near background of the Galactic Bulge, respectively. For R15, an RRab, its A_K is still within the uncertainty range of the mean extinction of the central parsec ($\sim 25''$), 2.54 ± 0.12 mag (Schödel et al. 2010). Therefore, R15 could lie in the Nuclear Bulge, close to Sgr A*, but we cannot say with certainty whether it belongs to the MWNSC.

On the other hand, we notice that R3 and R5, two RRabs, appear to be located at the GC within their respective distance uncertainties, but with A_K smaller than the corresponding values in the extinction map of Nogueras-Lara et al. (in preparation) by more than 14 sigma. From Fig. 1 and Fig. 2, we can see that R3 and R5 fall into the low stellar number density regions, which suggest the existence of dense molecular clouds in front of the MWNSC. Therefore, the extinction of R3 and R5 indicate that they should be in front of the dense molecular clouds, and then the MWNSC. In order to further investigate this dilemma, we give the relationship between DM, A_{K_s} and α in Fig. 8 for the four RRab stars, R3, R5, R15 and R16. The DM is anti-correlated with the slope and A_K . Therefore, one possible solution is that the R3 and R5 are indeed foreground and the extinction which they suffer follows a law more similar to that of the solar neighborhood rather than a steep extinction law with $\alpha = -2.2$. From Table 3 and Fig. 8, we can see that for α less negative than -2.0, R3 and R5 could still have extinctions smaller than the values given in Schödel et al. (2010) and be closer to us than the MWNSC.

The distances of the other six RRL stars indicate that they are at the foreground or background of the MWNSC. R2 and R8, having extinctions smaller than those in the extinction map, are RRcs in front of the MWNSC. R7, R9, R11 and R16 are behind the MWNSC, but have smaller extinction than indicate by the extinction map. In particular, R16 is a typical RRab star. A possible explanation is the clumpiness of the molecular gas in the circumnuclear ring.

Minniti et al. (2016) found 14 RRL stars within the central $36'$ (86 pc) from the VVV survey in the J , H and K bands. Assuming that the intrinsic color of RRL stars is $(J-K)_o = 0.15$ mag, they derived the extinction $(E(J-K))$. Then they used different versions of extinction curves and PL relationships for RRL stars to derive their distances. They

claimed that 12 of the RRL stars lie within the Nuclear Bulge. However, we notice that the extinction values of their RRLs range between $A_{K_s} = 1.06$ and 1.8, which are significantly smaller than what we expect for the Nuclear Bulge. For example, Dong et al. (2011) produce an extinction map with $4''$ resolution from *HST*/NICMOS observations covering the central $39' \times 15'$. The median and 68th percentile of A_K derived from this map are 2.3 and [2.0, 2.75]. Also, the extinction map of the Nuclear Bulge presented by Schödel et al. (2014) suggests values $A_K > 2.0$ for most of the Nuclear Bulge. According to Tables 1 and 2 of Minniti et al. (2016), only five of their RRLs fall in projection onto the region of the Nuclear Stellar Disk and only two of them (IDs, 37068 and 33007) are within 500 pc of Sgr A* along the line-of-sight. The A_K values of these two stars are 1.23 and 1.44 mag. Therefore, it is more likely that these RRL stars are part of the foreground Galactic Bulge, instead of the MWNSC.

4.2. RRL population in the MWNSC?

Although we have identified only one well-defined RRab, R15, that could plausibly belong to the MWNSC, we expect that the MWNSC potentially contains a much larger number of such stars that are not detected in our study. In Paper I, we divided our field-of-view into ten regions, according to the local surface brightness. R15 falls into the #5 region (the larger the number, the higher the surface brightness) with a 50% completeness limit of $F153M = 19.2$ mag. RRL stars with similar magnitudes would not be detected in regions #7-10, with 50% completeness limits < 18 mag. In addition to the source confusion, the strong extinction is another limiting factor for the detection. On average, the lower surface brightness represents regions with greater foreground extinction. This will make it extreme difficult to detect RRLs that are located in the MWNSC and are behind the clouds that are responsible for the high extinction. Of course, our estimate of the RRL population in the MWNSC also needs to consider the stellar spatial distribution of the cluster, relative to the foreground and background across the field.

We performed simulations to estimate the detection fraction of RRab stars in the MWNSC. We assumed that the distribution of RRL stars follows the surface brightness distribution as described by Eqn. 1 of Fritz et al. (2016) with their Model No 4 parameters in their Table 1². Then, we added the distance modulus to the absolute magnitude of R15 and applied the appropriate extinction. We adopted the R15's light curve as a template. In

²This equation includes also the contribution from the Galactic Nuclear Disk, but which is small in our field-of-view.

order to simulate the observations, we randomly chose starting phases of the light curve and assigned the photometric errors by using the information giving in §2.1. The completeness as a function of input magnitude from the artificial star tests applied to the ten regions (Fig. 5 of Paper I) was used to determine whether the RRL stars can be detected or not. We then applied the least-chi-square method described in Paper I to check whether each detected source may be identified as a variable. We performed 10,000 such simulations for each of total ‘N_tot’ RRab stars. Fig. 9 shows the median fraction of the recovered variable stars, as well as its 65%, 90%, 99% percentiles. From this plot, we conclude that the median detection fraction is ~ 0.1 and exclude $N_{\text{tot}} > 40$ with 90% confidence.

4.3. Old stellar population in the MWNSC?

Finally, we use the number of RRab stars to estimate the potential contribution of an old, metal poor population to the MWNSC, which could have been brought into the GC by the infall of globular clusters. Mateu et al. (2009) show that the numbers of RRab stars in dSph satellite galaxies of the Milky Way and M31 are strongly correlated with the galaxies’ absolute magnitudes. For a constant mass-to-light ratio, we also expect a tight correlation between the number of RRab stars and the total stellar mass of dSph galaxies.

We tested this relation on Milky Way globular clusters. We used the variable star catalog for globular clusters given by Clement et al. (2001)³. We only selected sources with variable types equal to ‘R0’, ‘RR0’, ‘RR0?’ (all are RRab stars, according to the draft classification for the 2006 version of General Catalog of Variable Stars). The total masses and metallicities of globular clusters were taken from Gnedin & Ostriker (1997) and Harris (1996), respectively. We divide the globular clusters into OoI and OoII clusters according to their metallicities. For these two groups, we found 30 and 41 globular clusters in Clement et al. (2001) with measured total stellar masses and detected RRab star(s)⁴. Fig. 10 shows the correlation between the total cluster masses and the numbers of RRab stars for these two groups of clusters, although the scatters are large. Based on these star clusters, we obtained the

³online catalogs: <http://www.astro.utoronto.ca/~cclement/read.html>. The catalogs have been continuously updated by the authors. We used the data updated on March 22, 2017.

⁴Four and six clusters in these two groups do not have detected RRab star for two reasons: 1) small total masses: NGC 6325 ($9.6 \times 10^4 M_{\odot}$), Palomar 4 ($5.4 \times 10^4 M_{\odot}$) and NGC 6287 ($1.0 \times 10^5 M_{\odot}$) and 2) no available high-quality time-domain studies: NGC 6218, NGC 6517, NGC 4372, NGC 5694, NGC 6144, NGC 6254 and NGC 6752.

following relationship:

$$\begin{aligned} \log(\text{cluster mass}(M_{\odot})) &= 5.13 \pm 0.12 + (0.33 \pm 0.09) \times \log(\text{number of RRab}); \text{ for OoI(11)} \\ \log(\text{cluster mass}(M_{\odot})) &= 5.05 \pm 0.15 + (0.34 \pm 0.14) \times \log(\text{number of RRab}); \text{ for OoII(12)} \end{aligned}$$

with a standard deviation of 0.29 dex and 0.48 dex, respectively.

By using the relations above, we could estimate the contribution of infall globular clusters in the MWNSC. The Bailey diagram in Fig. 7 shows that the four likely RRab stars and three RRab candidates lie close to the OoI line, like most of the RRab stars in the Galactic Bulge (Gran et al. 2016). This means that our newly identified RRL stars probably have metallicities $-1.5 < [\text{Fe}/\text{H}] < -1$. Therefore, using the relationship above for the OoI clusters, we could estimate that 10 and 40 RRab stars – our best estimated number and the 90% upper limit for the MWNSC, respectively – correspond to globular clusters with masses of 2.9×10^5 [2.1×10^5 , 4.1×10^5] M_{\odot} and 4.7×10^5 [3.1×10^5 , 7.2×10^5] M_{\odot} (68% uncertainty intervals). We can compare this value with the stellar mass of the MWNSC in our field-of-view, $\sim 2.6 \times 10^6 M_{\odot}$, as estimated from Table 8 of Fritz et al. (2016). We conclude that the old metal-poor population contributed by the OoI cluster occupies at most 18% of the total mass of the MWNSC in this region, because both infall globular cluster and ancient *in situ* star formation could provide these old metal-poor stars. This is consistent with the low fraction ($\sim 5\%$) of metal-poor stars ($-1.5 < [\text{Fe}/\text{H}] < -0.5$) in the MWNSC found by Do et al. (2015) and Feldmeier-Krause et al. (2017).

On the other hand, we do not detect any RRab stars, which fall into the OoII region in the Bailey diagram. These RRab stars have slightly longer periods (the average period is ~ 0.65 d, Catelan 2009) than the ones in OoI clusters (the average period is ~ 0.65 d). Therefore, if they existed in the MWNSC and were detected in our dataset, their periods could be accurately determined. The existence of OoII clusters in the MWNSC is also inconsistent with the minimum stellar abundance reported by Do et al. (2015) and Feldmeier-Krause et al. (2017): -1.27 dex and -1.25 dex. According to Fig. 9 and the relationship above for the OoII cluster, the 90% upper limit for the total mass of the OoII clusters is $3.3 \times 10^5 M_{\odot}$, i.e. 13% of the total mass of the MWNSC.

5. Summary

In this paper, we have performed a study of 21 variable stars with periods between 0.2 and 1 d identified in *HST* WFC3/IR F153M observations of the Milky Way nuclear star cluster (Dong et al. 2017, Paper I). We have analyzed their light curves and studied their extinctions and distances. Based on these analyses, we have typed the variable stars,

estimated their physical locations, and discussed the implications of the results, focusing on the RRL stars in the MWNSC. Our findings are the following:

- The 21 sources are classified as: four RRc stars, four RRab stars, three RRab candidates and ten eclipsing binaries. In particular, our RRab stars are ~ 2 mag dimmer and should be closer to the Galactic Nuclear Bulge than those identified in Minniti et al. (2016).
- Using the well-defined period-luminosity function from the literature, we calculate the line-of-sight distances of our 11 RRL stars to be ~ 4 kpc to 11 kpc away from us.
- All four well defined RRab stars and three RRab candidates fall onto the Oosterhoff I division, which suggests that the old stellar population near the GC is relatively metal-rich with $-1.5 < [\text{Fe}/\text{H}] < -1$ and could have the same origin as the old stellar population in the Galactic Bulge.
- We have found that only one out of our four well-defined RRab stars may actually belong to the MWNSC or lie in the inner Nuclear Bulge. With simulations, we estimate that there could be at most 40 RRab stars in the MWNSC. From the observed RRL star population per unit mass in globular clusters, we conclude that an old, metal poor (with $-1.5 < [\text{Fe}/\text{H}] < -1$) population, possibly contributed to the MWNSC by globular cluster infall, cannot make up more than about 18% of its mass. The non-detection of RRab stars from OoII clusters puts an even stronger constraint on the fraction of stars with even lower ($-2.5 < [\text{Fe}/\text{H}] < -1.5$) metallicities: They can contribute at most 13% of the total mass of the MWNSC. Of course, old metal poor stars may also have formed in the MWNSC *in situ*. This would reduce the contribution to this population from globular cluster infall even further.

Acknowledgments

We thank the anonymous referee for a thorough, detailed, and constructive commentary on our manuscript. The research leading to these results has received funding from the European Research Council under the European Union’s Seventh Framework Programme (FP7/2007-2013) / ERC grant agreement n [614922]. The work is also supported partly by NASA via the grant GO-14589, provided by the Space Telescope Science Institute. F N-L acknowledges financial support from a MECD predoctoral contract, code FPU14/01700. This work uses observations made with the NASA/ESA Hubble Space Telescope and the data archive at the Space Telescope Science Institute, which is operated by the Association

of Universities for Research in Astronomy, Inc. under NASA contract NAS 5-26555. We are grateful to Zhiyuan Li, Francisco Najarro, Jon Mauerhan, Farhad Yusef-Zadeh and Stephen Eikenberry for many valuable comments and discussion.

A. Transformation from the Johnson-Cousins-Glass to *HST* WFC3/IR Magnitudes

Catelan et al. (2004) give the M_J and M_H of RR Lyrae stars in the Johnson-Cousins-Glass system. In order to derive the absolute extinctions and the distance moduli for the RRL stars in § 2.3, we need to translate M_J and M_H into the *HST* WFC3/IR M_{F127M} and M_{F153M} magnitudes.

We used the stellar atmosphere models by Castelli & Kurucz (2004), the transmission curves of J and H bands of the Johnson-Cousins-Glass system and the F127M and F153M bands of *HST* WFC3/IR distributed in SYNPHOT package provided by STScI to derive the relationship. According to Marconi et al. (2015), the surface temperature of RR Lyrae stars is between 5500 K to 8000 K. Therefore, we only used the stellar atmosphere models with this temperature range and also metallicity ≤ 0.02 (solar metallicity) and surface gravity, $\log g \leq 3$. The SYNPHOT package is used to derive the intensities of these stellar atmosphere models in units of Jy at these four bands. Then, we derived the zero-points in units of Jy from the Vega spectrum also provided in the SYNPHOT package, which are used to convert the intensities of the stellar atmosphere models into magnitudes. We used the least chi-square method to derive the following translation:

$$M_{F127M} = M_J - 0.0059 - 0.1678 \times (M_J - M_H) \tag{A1}$$

$$M_{F153M} = M_H + 0.0208 + 0.0793 \times (M_J - M_H) \tag{A2}$$

$$\tag{A3}$$

The difference between M_{F127M} (M_{F153M}) and the ones derived from the equations above from M_J and M_H are less than 0.008 (0.014) mag for the entire range of stellar parameters of RRL stars.

B. Converting α to the relative extinction

We used the same method given in Appendix A to derive the relative extinction A_{F127M}/A_{Ks} and A_{F153M}/A_{Ks} for different α . We assumed that the temperature and the logarithm surface gravity of RRL stars are 6500 K and 2.5 and used the corresponding atmosphere models

from Castelli & Kurucz (2004). We first red the spectrum by the extinction curves with different slopes and absolute extinctions. Then the ‘SYNPHOT’ package is used to derive the magnitudes at the F127M and F153M magnitude, as well as VLT/NACO Ks band. After that, by subtracting the magnitudes at these three bands without foreground extinction, respectively, we derive the A_{F127M} , A_{F153M} and A_{Ks} . Finally, we can calculate the mean of A_{F127M}/A_{Ks} and A_{F153M}/A_{Ks} for various foreground extinctions with different α .

REFERENCES

- Agarwal, M. & Milosavljevi, M. 2011, ApJ, 729, 35
- Antonini, F., Capuzzo-Dolcetta, R., Mastrobuono-Battisti, A. & Merritt, D. 2011, ApJ, 750, 111
- Bekki, K., Couch, W. J., & Shioya, Y. 2006, ApJ, 642, L133
- Boehle, A., Ghez, A. M., Schödel, R., et al. 2016, ApJ, 830, 17
- Böker, T., Laine, S., van der Marel, R. P., et al. 2002, AJ, 123, 1389
- Böker, T., Sarzi, M., McLaughlin, D. E., et al. 2004, AJ, 127, 105
- Buchholz, R. M., Schödel, R., & Eckart, A. 2009, A&A, 499, 483
- Georgiev, I. Y., Böker, T., Leigh, N., Lützgendorf, N., & Neumayer, N. 2016, MNRAS, 457, 2122
- Carson, D. J., Barth, A. J., Seth, A. C., den Brok, M., Cappellari, M., Greene, J. E., Ho, L. C., & Neumayer, N. 2015, AJ, 149, 170
- Castelli, F., & Kurucz, R. L. 2004, arXiv:astro-ph/0405087
- Catelan, M., Pritzl, B. J., & Smith, H. A. 2004, ApJS, 154, 633
- Catelan, M. 2009, Ap&SS, 320, 261
- Catelan, M., Minniti, D., Lucas, P. W., et al. 2013, arXiv:1310.1996
- Chadid, M., Sneden, C. & Preston, G. W. 2016, arXiv 1611.02368
- Clement, C. M., Muzzin, A., Dufton, Q., et al. 2001, AJ, 122, 2587
- Dékány, I., Minniti, D., Catelan, M., et al. 2013, ApJ, 776, L19

- Dékány, I., Minniti, D., Majaess, D., et al. 2015, *ApJ*, 812, L29
- Do, T., Kerzendorf, W., Winsor, N., et al. 2015, *ApJ*, 809, 143
- Dolphin, A. E. 2000, *PASP*, 112, 1383
- Dong, H., Wang, Q. D., Cotera, A., et al. 2011, *MNRAS*, 417, 114
- Dong, H., Schödel, R., Williams, B. F., Nogueras-Lara, F., Gallego-Cano, E., Gallego-Calvente, T., Wang, Q. D., Morris, M. R., Do, T., Ghez, A., 2017, accepted by *MNRAS*, arxiv1706.03243
- Draine, B. T. 1989, *Infrared Spectroscopy in Astronomy*, 290,
- Feast, M. W., Laney, C. D., Kinman, T. D., van Leeuwen, F., & Whitelock, P. A. 2008, *MNRAS*, 386, 2115
- Feldmeier, A., Neumayer, N., Seth, A., et al. 2014, *A&A*, 570, A2
- Feldmeier-Krause, A., Kerzendorf, W., Neumayer, N., et al. 2017, *MNRAS*, 464, 194
- Fritz, T. K., Gillessen, S., Dodds-Eden, K., et al. 2011, *ApJ*, 737, 73
- Fritz, T. K., Chatzopoulos, S., Gerhard, O., et al. 2016, *ApJ*, 821, 44
- Gallego-Cano, E., Schödel, R., Dong, H., et al. 2017, arXiv:1701.03816
- Genzel, R., Eisenhauer, F., & Gillessen, S. 2010, *Reviews of Modern Physics*, 82, 3121
- Ghez, A. M., Salim, S., Weinberg, N. N., et al. 2008, *ApJ*, 689, 1044-1062
- Gillessen, S., Eisenhauer, F., Fritz, T. K., et al. 2009, *ApJ*, 707, L114
- Gillessen, S., Plewa, P., Eisenhauer, F., et al. 2016, arXiv:1611.09144
- Gnedin, O. Y., & Ostriker, J. P. 1997, *ApJ*, 474, 223
- Gosling, A. J., Bandyopadhyay, R. M., & Blundell, K. M. 2009, *MNRAS*, 394, 2247
- Gran, F., Minniti, D., Saito, R. K., et al. 2015, *A&A*, 575, A114
- Gran, F., Minniti, D., Saito, R. K., et al. 2016, *A&A*, 591, A145
- Harris, W. E. 1996, *AJ*, 112, 1487
- Groenewegen, M. A. T. 2008, *A&A*, 488, 935

- Hartmann, M., Debattista, V. P., Seth, A., Cappellari, M. & Quinn, T. R. 2011 MNRAS 418, 2697
- Hosek, M. W., Jr., Lu, J. R., Anderson, J., et al. 2015, ApJ, 813, 27
- Jurcsik, J., & Kovacs, G. 1996, A&A, 312, 111
- Lau, R. M., Herter, T. L., Morris, M. R., Becklin, E. E., & Adams, J. D. 2013, ApJ, 775, 37
- Launhardt, R., Zylka, R., & Mezger, P. G. 2002, A&A, 384, 112
- Lee, Y.-W. 1992, AJ, 104, 1780
- Lomb, N. R. 1976, Ap&SS, 39, 447
- Longmore, A. J., Dixon, R., Skillen, I., Jameson, R. F., & Fernley, J. A. 1990, MNRAS, 247, 684
- Lotz, J. M., Telford, R., Ferguson, H. C., et al. 2001, ApJ, 552, 572
- Lu, J. R., Do, T., Ghez, A. M., et al. 2013, ApJ, 764, 155
- Kovács, G., & Kupi, G. 2007, A&A, 462, 1007
- Mateu, C., Vivas, A. K., Zinn, R., Miller, L. R., & Abad, C. 2009, AJ, 137, 4412
- Marconi, M., Coppola, G., Bono, G., et al. 2015, ApJ, 808, 50
- Matsunaga, N., Feast, M. W., Bono, G., et al. 2016, MNRAS, 462, 414
- Minniti, D., Lucas, P. W., Emerson, J. P., et al. 2010, New A, 15, 433
- Minniti, D., Contreras Ramos, R., Zoccali, M., et al. 2016, ApJ, 830, L14
- Mossoux, E., Grosso, N., Bushouse, H., et al. 2016, A&A, 589, A116
- Navarrete, C., Contreras Ramos, R., Catelan, M., et al. 2015, A&A, 577, A99
- Neumayer, N., Walcher, C. J., Andersen, D., Sanchez, S. F., Bker, T. & Rix, H.-W. 2011, MNRAS, 413, 1875
- Nishiyama, S., et al. 2006, ApJ, 638, 839
- Paumard, T., Genzel, R., Martins, F., Nayakshin, S., Beloborodov, A. M., Levin, Y., Trippe, S., Eisenhauer, F., Ott, T., Gillessen, S., Abuter, R., Cuadra, J., Alexander, T. & Sternberg, A. 2006, ApJ, 643, 1011

- Pfuhl, O., Fritz, T. K., Zilka, M., et al. 2011, *ApJ*, 741, 108
- Pietrukowicz, P., Udalski, A., Soszyński, I., et al. 2012, *ApJ*, 750, 169
- Pietrukowicz, P. and the OGLE collaboration 2016, *Proc. IAU Symposium 317*, eds. A. Bragaglia, M. Arnaboldi, M. Rejkuba & D. Romano, 116
- Puzeras, E., Tautvaišienė, G., Cohen, J. G., et al. 2010, *MNRAS*, 408, 1225
- Ryde, N., & Schultheis, M. 2015, *A&A*, 573, A14
- Scargle, J. D. 1982, *ApJ*, 263, 835
- Schdel, R., Eckart, A., Alexander, T., Merritt, D., Genzel, R., Sternberg, A., Meyer, L., Kul, F., Moulta, J., Ott, T. & Straubmeier, C. 2007, *A&A*, 469, 125
- Schödel, R., Merritt, D., & Eckart, A. 2009, *A&A*, 502, 91
- Schödel, R., Najarro, F., Muzic, K., & Eckart, A. 2010, *A&A*, 511, A18
- Schödel, R., Feldmeier, A., Kunneriath, D., et al. 2014, *A&A*, 566, A47
- Schdel, R., Feldmeier, A., Neumayer, N., Meyer, L. & Yelda, S. 2014, *Classical and Quantum Gravity*, 31, 244007
- Schödel, R., Gallego-Cano, E., Dong, H., et al. 2017, arXiv:1701.03817
- Schultheis, M., Ryde, N., & Nandakumar, G. 2016, *A&A*, 590, A6
- Smolec, R. 2005, *Acta Astron.*, 55, 59
- Støstad, M., Do, T., Murray, N., et al. 2015, *ApJ*, 808, 106
- Tremaine, S. D., Ostriker, J. P., & Spitzer, L., Jr. 1975, *ApJ*, 196, 407
- Walcher, C. J., van der Marel, R. P., McLaughlin, D., et al. 2005, *ApJ*, 618, 237
- Walcher, C. J., Böker, T., Charlot, S., et al. 2006, *ApJ*, 649, 692
- Walker, A. R. 1989, *PASP*, 101, 570
- Walker, A. R., & Terndrup, D. M. 1991, *ApJ*, 378, 119
- Yusef-Zadeh, F., Roberts, D. A., Wardle, M., Cotton, W., Schdel, R. & Royster, M. J. (2015), *ApJ*, 801, L26

Table 1. Source Catalog

| Name | ID ^a | RA | Dec | F127M ^{b,c} | $\langle F127M \rangle$ | F153M ^{c,d} | $\langle F153M \rangle$ | $\frac{\langle F127M \rangle}{-\langle F153M \rangle^e}$ | Period ^f | Type |
|------|-----------------|-----------|-----------|--|-------------------------|--|-------------------------|--|---------------------|------------|
| R1 | 2495 | 266.41349 | -29.00661 | 17.2 ^{+0.01} _{-0.01} | 17.2 | 16.6 ^{+0.07} _{-0.07} | 16.6 | 0.56 ^{+0.01} _{-0.03} | 0.542 | Ecl? |
| R2 | 7831 | 266.42698 | -28.99449 | 20.6 ^{+0.04} _{-0.03} | 20.6 | 17.7 ^{+0.10} _{-0.09} | 18.1 | 2.51 ^{+0.02} _{-0.02} | 0.299 | RRc |
| R3 | 8735 | 266.42807 | -29.00793 | 20.3 ^{+0.07} _{-0.06} | 20.2 | 18.0 ^{+0.13} _{-0.11} | 18.1 | 2.09 ^{+0.04} _{-0.05} | 0.559 | RRab |
| R4 | 9074 | 266.42224 | -28.99591 | 20.2 ^{+0.02} _{-0.02} | 20.0 | 18.1 ^{+0.11} _{-0.09} | 18.1 | 1.85 ^{+0.02} _{-0.02} | 0.838 | Ecl? |
| R5 | 10520 | 266.43683 | -29.00501 | 20.3 ^{+0.06} _{-0.05} | 20.4 | 18.2 ^{+0.12} _{-0.11} | 18.3 | 2.12 ^{+0.06} _{-0.07} | 0.542 | RRab |
| R6 | 12097 | 266.42163 | -28.99880 | 21.3 ^{+0.04} _{-0.03} | 21.3 | 18.4 ^{+0.12} _{-0.10} | 18.5 | 2.78 ^{+0.03} _{-0.03} | 0.489 | RRab?/Ecl? |
| R7 | 13950 | 266.39578 | -29.00507 | 21.2 ^{+0.11} _{-0.10} | 21.2 | 18.6 ^{+0.16} _{-0.14} | 18.8 | 2.39 ^{+0.06} _{-0.07} | 0.686 | RRab? |
| R8 | 14123 | 266.43548 | -29.01042 | 21.3 ^{+0.06} _{-0.05} | 21.3 | 18.6 ^{+0.15} _{-0.13} | 18.8 | 2.53 ^{+0.05} _{-0.05} | 0.384 | RRc |
| R9 | 14583 | 266.43086 | -28.99710 | 21.3 ^{+0.10} _{-0.09} | 21.3 | 18.8 ^{+0.15} _{-0.12} | 18.9 | 2.37 ^{+0.06} _{-0.06} | 0.677 | RRab? |
| R10 | 15242 | 266.41267 | -29.01958 | 20.7 ^{+0.08} _{-0.07} | 20.7 | 18.8 ^{+0.17} _{-0.14} | 19.0 | 1.74 ^{+0.04} _{-0.04} | 0.329 | Ecl? |
| R11 | 19440 | 266.41636 | -28.99466 | 21.5 ^{+0.12} _{-0.11} | 21.5 | 18.9 ^{+0.19} _{-0.15} | 19.4 | 2.02 ^{+0.07} _{-0.08} | 0.294 | RRc |
| R12 | 20993 | 266.40610 | -28.99370 | 21.7 ^{+0.05} _{-0.04} | 21.8 | 18.9 ^{+0.17} _{-0.14} | 19.7 | 2.17 ^{+0.06} _{-0.06} | 0.368 | Ecl? |
| R13 | 21740 | 266.41443 | -28.99120 | 22.0 ^{+0.09} _{-0.08} | 22.0 | 19.5 ^{+0.21} _{-0.17} | 19.6 | 2.40 ^{+0.07} _{-0.09} | 0.244 | RRc |
| R14 | 22081 | 266.42041 | -28.99793 | 22.4 ^{+0.08} _{-0.07} | 22.3 | 19.6 ^{+0.17} _{-0.14} | 19.7 | 2.62 ^{+0.07} _{-0.08} | 0.495 | RRab?/Ecl? |
| R15 | 22197 | 266.41891 | -28.99733 | 22.8 ^{+0.08} _{-0.07} | 22.7 | 19.7 ^{+0.16} _{-0.14} | 19.8 | 2.96 ^{+0.07} _{-0.08} | 0.593 | RRab |
| R16 | 22312 | 266.40715 | -29.02182 | 22.4 ^{+0.15} _{-0.13} | 22.5 | 19.8 ^{+0.26} _{-0.20} | 19.8 | 2.63 ^{+0.08} _{-0.09} | 0.573 | RRab |
| R17 | 23037 | 266.40810 | -28.99731 | 22.2 ^{+0.21} _{-0.18} | 22.1 | 19.8 ^{+0.30} _{-0.22} | 20.0 | 2.13 ^{+0.11} _{-0.12} | 0.469 | Ecl? |
| R18 | 25542 | 266.42178 | -29.01424 | 22.2 ^{+0.24} _{-0.20} | 22.3 | 19.8 ^{+0.30} _{-0.22} | 20.4 | 1.93 ^{+0.14} _{-0.16} | 0.258 | Ecl? |
| R19 | 25912 | 266.42983 | -29.00620 | 23.7 ^{+0.19} _{-0.16} | 23.7 | 19.9 ^{+0.31} _{-0.22} | 20.5 | 3.27 ^{+0.09} _{-0.11} | 0.644 | RRab? |
| R20 | 26822 | 266.42686 | -29.01960 | 22.9 ^{+0.11} _{-0.10} | 22.8 | 20.0 ^{+0.19} _{-0.16} | 20.5 | 2.28 ^{+0.08} _{-0.09} | 0.722 | Ecl? |
| R21 | 28701 | 266.40033 | -28.99777 | 22.7 ^{+0.23} _{-0.19} | 23.0 | 20.0 ^{+0.29} _{-0.21} | 20.9 | 2.10 ^{+0.11} _{-0.13} | 0.235 | Ecl? |

Note. — ^a ID from the Table 3 of Paper I; ^b the F127M magnitudes could be different from Table 3 of Paper I, because Table 3 of Paper I gives the mean F127M magnitudes of Program GO-11671 and GO-12182, while in this table, we primary used the magnitudes from Program 11671, if not, then GO-12182; ^c The photometric uncertainties are from Table 3 of Paper I, which includes both systematic and statistic errors. The former is the bias introduced by crowding, which makes the stars artificially brighter; ^d from Table 3 of Paper I, the average magnitude of the observations from 2010 to 2014; ^e Because the stellar number density in the F153M band is higher than that in the F127M band due to the extinction, the bias introduced by the crowding makes the detected color systematically redder; ^f in units of days

Table 2. Results of Direct Fourier Fitting

| Name | Amplitude ^a | A_1 | ϕ_1 | A_{21} | ϕ_{21} | A_{31} | ϕ_{31} | A_{41} | ϕ_{41} | A_{51} | ϕ_{51} | A_{61} | ϕ_{61} |
|------|------------------------|-------|----------|----------|-------------|----------|-------------|----------|-------------|----------|-------------|----------|-------------|
| R1 | 0.05 | 0.024 | 4.869 | 0.000 | 0.000 | 0.000 | 0.000 | 0.000 | 0.000 | 0.000 | 0.000 | 0.000 | 0.000 |
| R2 | 0.07 | 0.049 | 3.970 | 0.353 | 4.786 | 0.000 | 0.000 | 0.000 | 0.000 | 0.000 | 0.000 | 0.000 | 0.000 |
| R3 | 0.10 | 0.112 | 0.411 | 0.337 | 4.169 | 0.194 | 1.823 | 0.102 | 5.680 | 0.029 | 2.481 | 0.000 | 0.000 |
| R4 | 0.26 | 0.141 | 2.689 | 0.304 | 4.691 | 0.114 | 3.472 | 0.056 | 2.300 | 0.063 | 0.615 | 0.000 | 0.000 |
| R5 | 0.33 | 0.128 | 4.852 | 0.392 | 3.962 | 0.250 | 1.505 | 0.189 | 5.271 | 0.101 | 2.539 | 0.097 | 6.196 |
| R6 | 0.33 | 0.054 | 2.373 | 0.205 | 4.569 | 0.000 | 0.000 | 0.000 | 0.000 | 0.000 | 0.000 | 0.000 | 0.000 |
| R7 | 0.11 | 0.063 | 3.714 | 0.153 | 4.057 | 0.062 | 2.468 | 0.000 | 0.000 | 0.000 | 0.000 | 0.000 | 0.000 |
| R8 | 0.12 | 0.049 | 1.847 | 0.000 | 0.000 | 0.000 | 0.000 | 0.000 | 0.000 | 0.000 | 0.000 | 0.000 | 0.000 |
| R9 | 0.13 | 0.047 | 5.282 | 0.245 | 4.270 | 0.000 | 0.000 | 0.000 | 0.000 | 0.000 | 0.000 | 0.000 | 0.000 |
| R10 | 0.10 | 0.073 | 3.807 | 0.082 | 4.283 | 0.049 | 4.648 | 0.038 | 0.060 | 0.000 | 0.000 | 0.000 | 0.000 |
| R11 | 0.10 | 0.086 | 4.356 | 0.168 | 4.650 | 0.000 | 0.000 | 0.000 | 0.000 | 0.000 | 0.000 | 0.000 | 0.000 |
| R12 | 0.15 | 0.100 | 0.498 | 0.184 | 4.554 | 0.037 | 3.352 | 0.000 | 0.000 | 0.000 | 0.000 | 0.000 | 0.000 |
| R13 | 0.17 | 0.079 | 4.928 | 0.208 | 5.023 | 0.000 | 0.000 | 0.000 | 0.000 | 0.000 | 0.000 | 0.000 | 0.000 |
| R14 | 0.22 | 0.081 | 4.399 | 0.145 | 5.316 | 0.000 | 0.000 | 0.000 | 0.000 | 0.000 | 0.000 | 0.000 | 0.000 |
| R15 | 0.21 | 0.095 | 0.802 | 0.369 | 4.367 | 0.169 | 2.029 | 0.096 | 6.114 | 0.000 | 0.000 | 0.000 | 0.000 |
| R16 | 0.16 | 0.128 | 4.139 | 0.447 | 4.054 | 0.282 | 1.552 | 0.202 | 5.255 | 0.129 | 3.061 | 0.088 | 0.306 |
| R17 | 0.16 | 0.132 | 1.811 | 0.206 | 4.778 | 0.090 | 2.787 | 0.041 | 1.039 | 0.000 | 0.000 | 0.000 | 0.000 |
| R18 | 0.22 | 0.161 | 5.156 | 0.185 | 4.799 | 0.060 | 3.970 | 0.000 | 0.000 | 0.000 | 0.000 | 0.000 | 0.000 |
| R19 | 0.34 | 0.071 | 3.387 | 0.339 | 3.450 | 0.277 | 0.767 | 0.133 | 3.370 | 0.000 | 0.000 | 0.000 | 0.000 |
| R20 | 0.29 | 0.067 | 0.244 | 0.417 | 5.058 | 0.329 | 3.074 | 0.375 | 1.481 | 0.372 | 0.379 | 0.275 | 5.803 |
| R21 | 0.25 | 0.229 | 2.877 | 0.252 | 4.800 | 0.101 | 3.215 | 0.092 | 1.348 | 0.046 | 6.030 | 0.000 | 0.000 |

Note. — ^a in units of mag

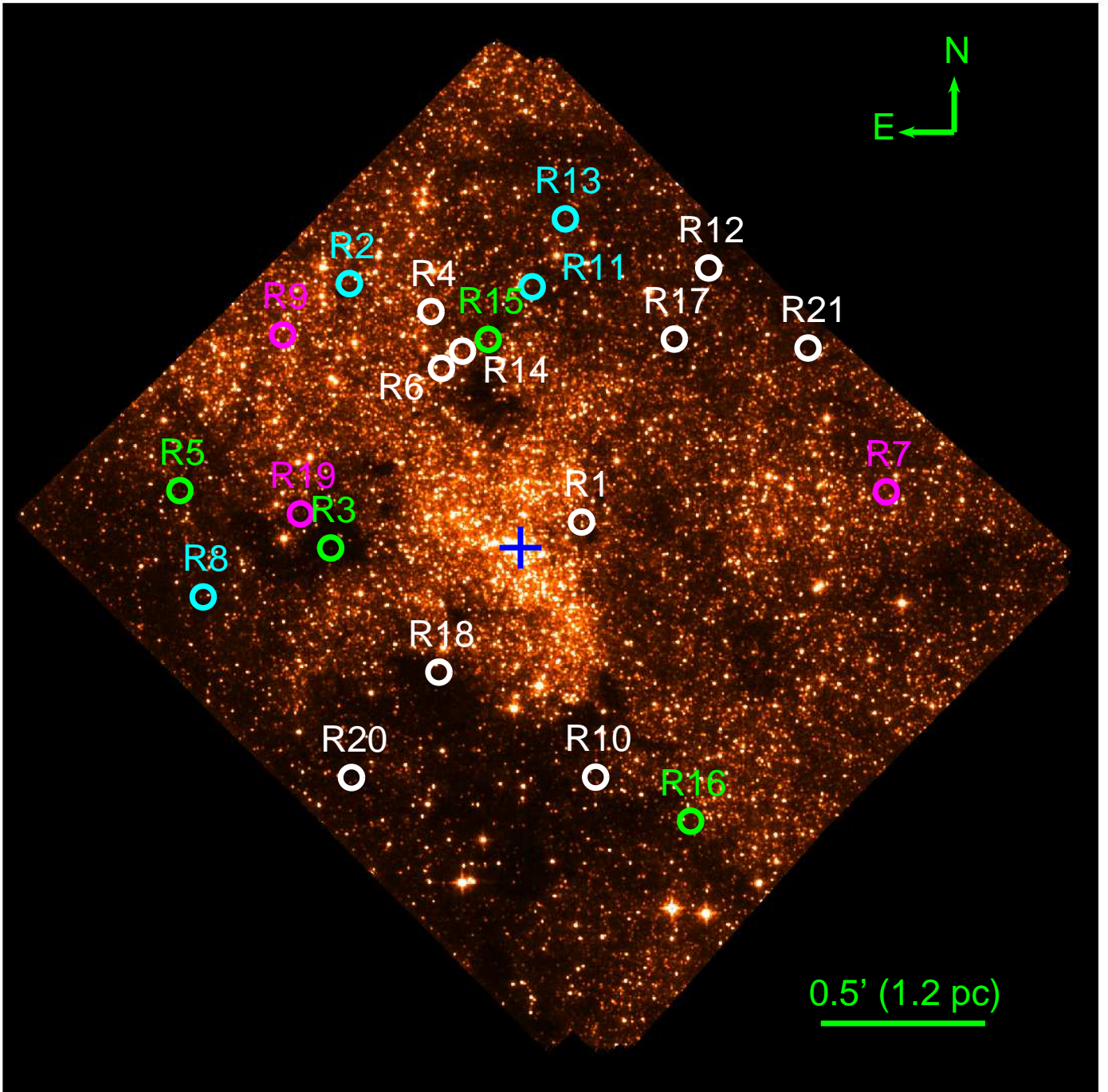


Fig. 1.— *HST* WFC3/IR F153M observations of the MWNSC. The blue plus marks the central massive black hole, Sgr A*. The green circles are the four variables with typical R_{Rab} light curves. The cyan circles mark R_{Rc} candidates, magenta ones R_{Rab} candidates, and white ones eclipsing binary candidates.

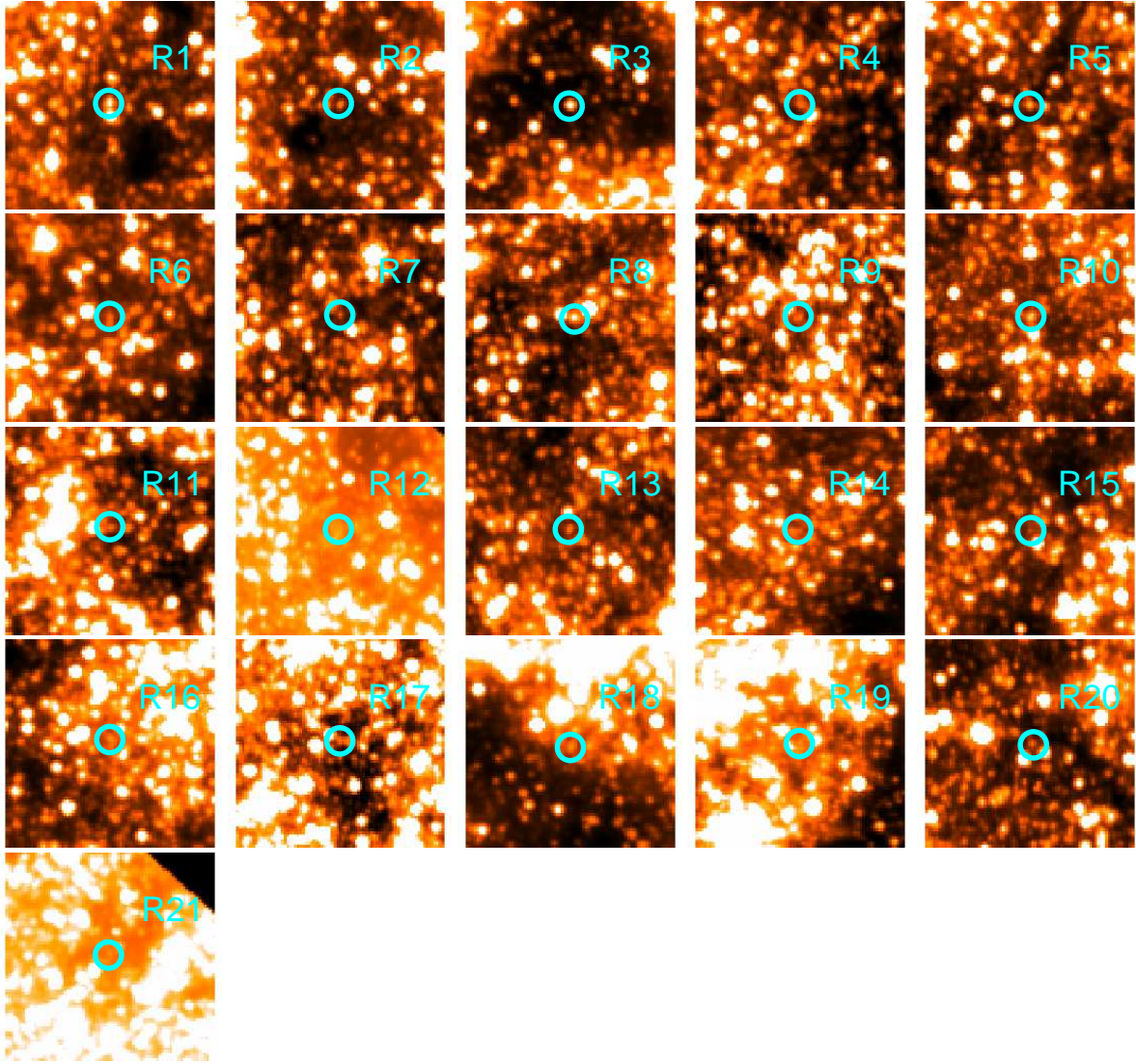


Fig. 2.— Detailed images of the surroundings of each star in our sample. The size of each map is $10'' \times 10''$.

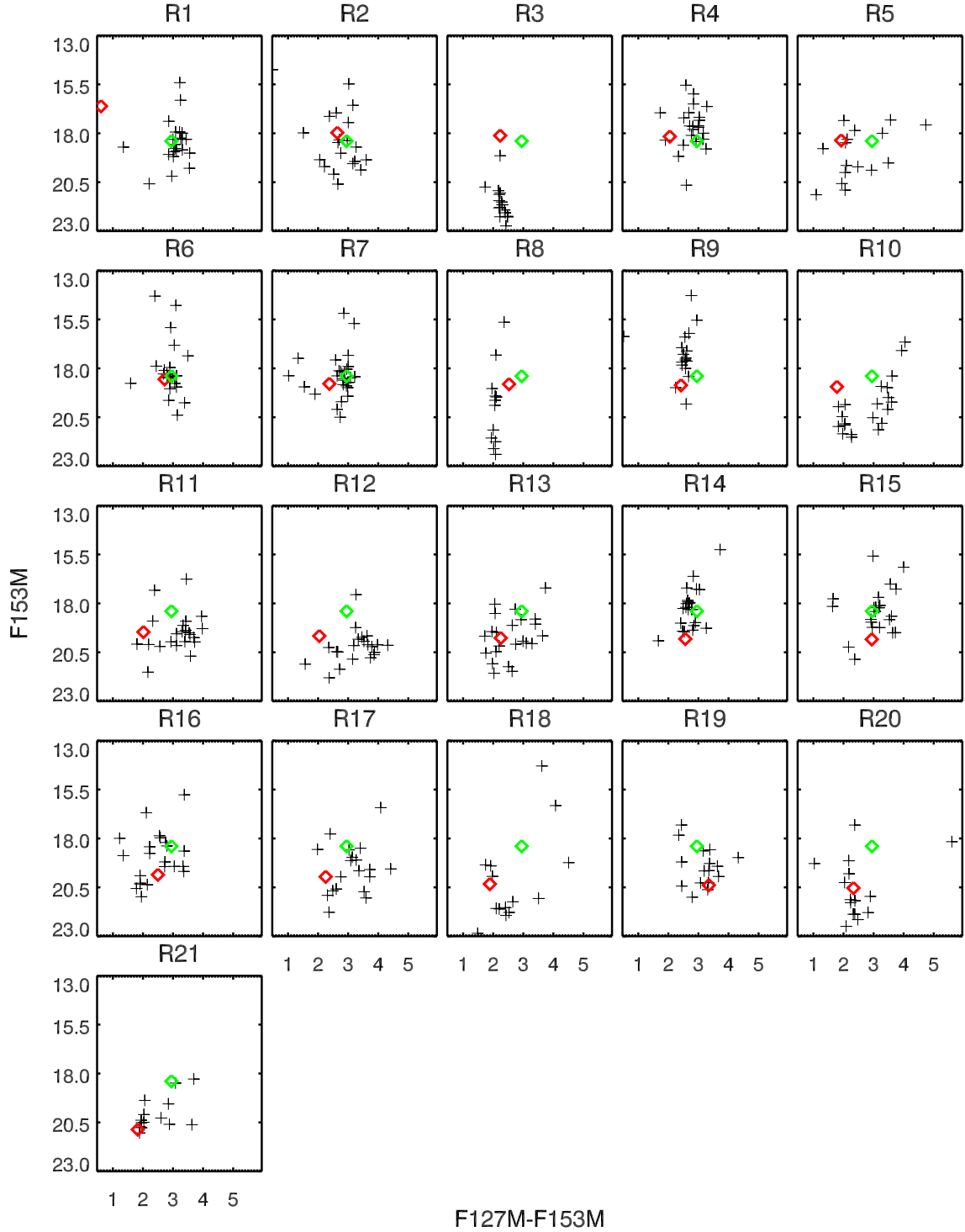


Fig. 3.— The colour magnitude diagram (F127M-F153M vs. F153M) of the detected sources (pluses) within $2''$ of the 21 RRL candidates (red diamonds). The green diamonds represent the location of the RC giants in the MWNSC with surface temperature $T_{eff}=4750K$, gravity $\log g=2.5$ (Puzeras et al. 2010), solar metallicity, $M_K=-1.54$ mag (Groenewegen 2008) and $A_K=2.5$ (Schödel et al. 2010).

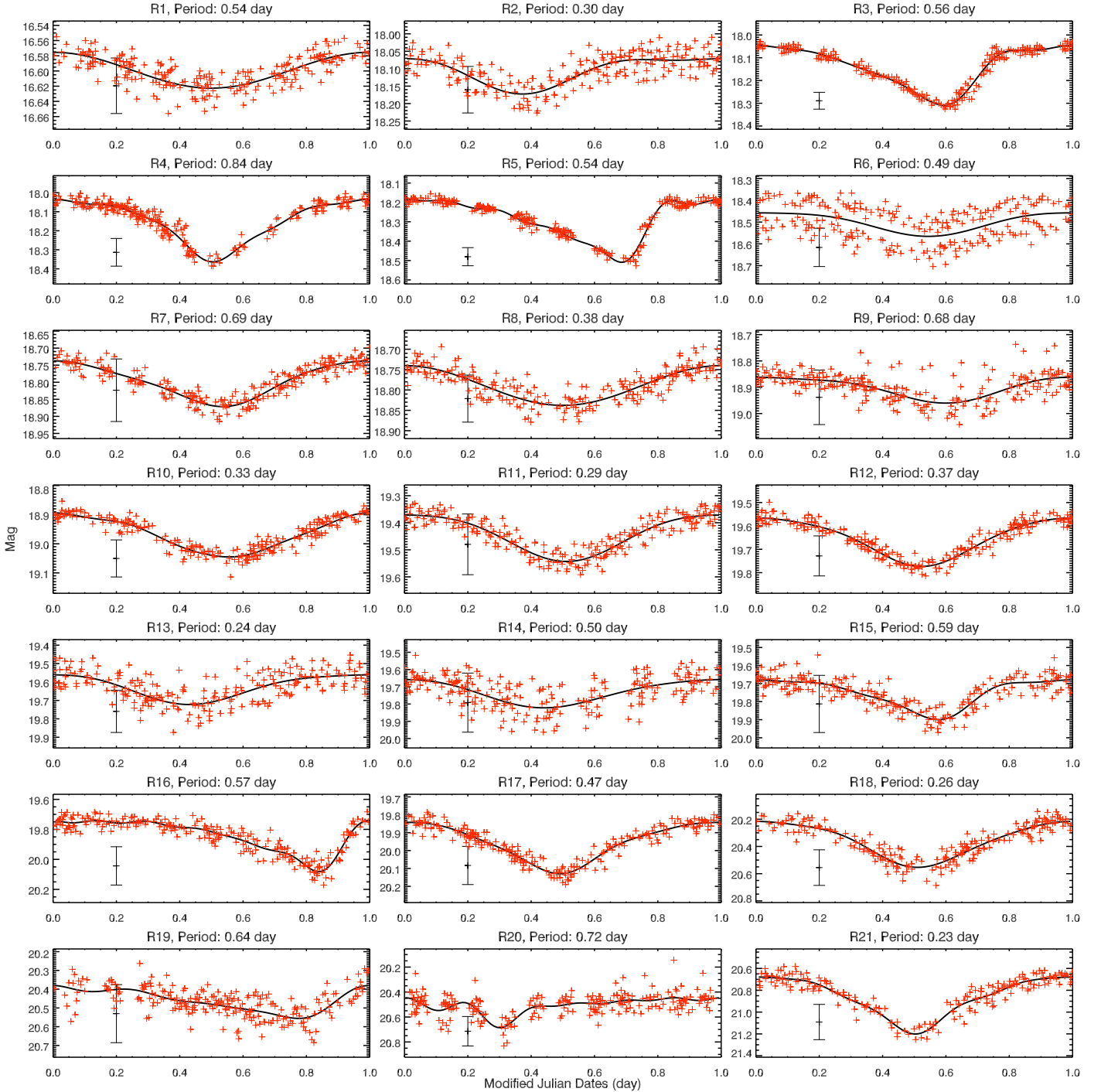


Fig. 4.— The folded F153M light curves for 21 sources. In the title of each figure, we give the source IDs and periods. The black pluses in the left bottom corner of the individual panels show the average photometric variation among dithered exposures derived from the artificial star tests, plus 0.01 mag systematic uncertainty (see Paper I for more details). The black solid lines are from the DFF fitting.

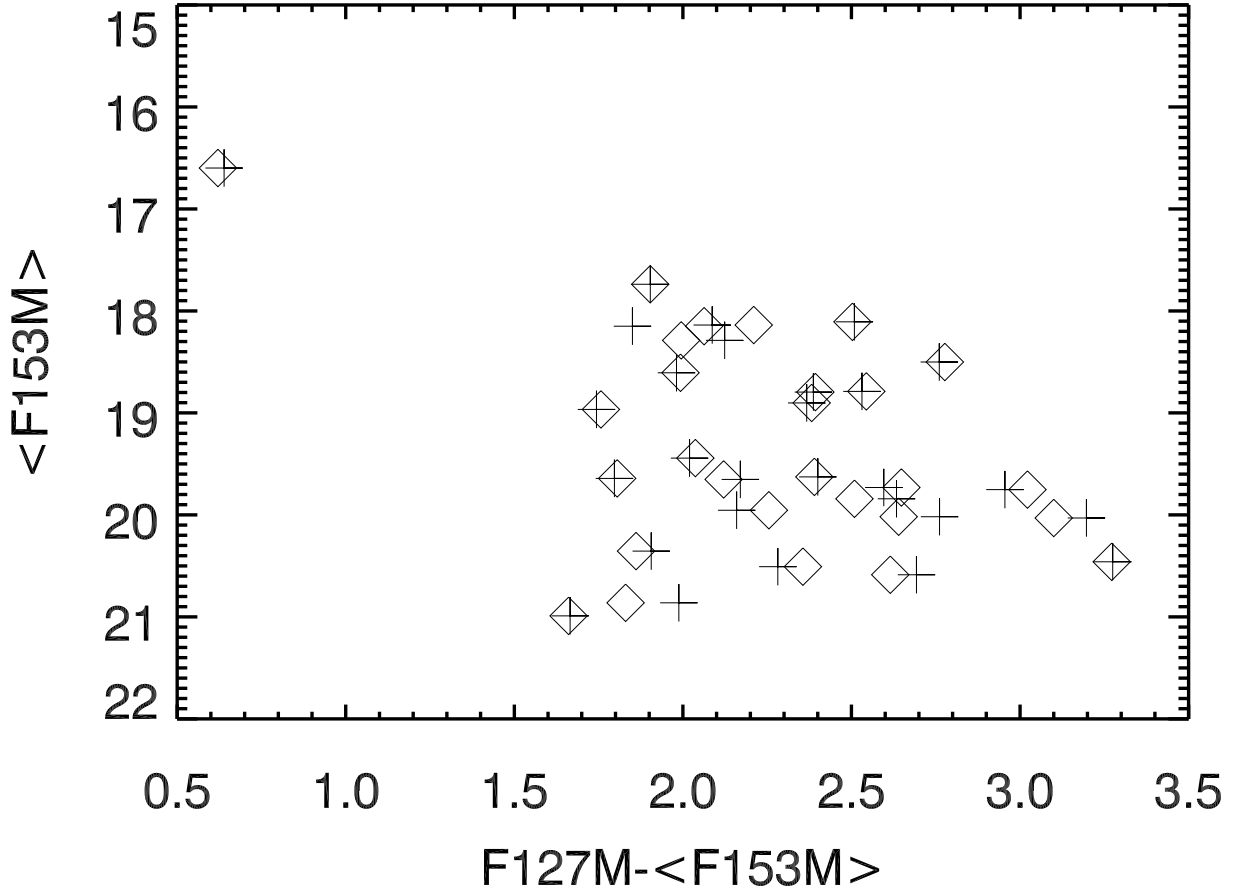


Fig. 5.— The $(F_{127M} - \langle F_{153M} \rangle)$ vs. $\langle F_{153M} \rangle$ CMD for the 21 RRL candidates. The diamond and cross symbols represent the observed F_{127M} magnitude and the mean F_{127M} magnitude, $\langle F_{127M} \rangle$, after the phase correction with the light curves from the F_{153M} band (see more details in §2.3).

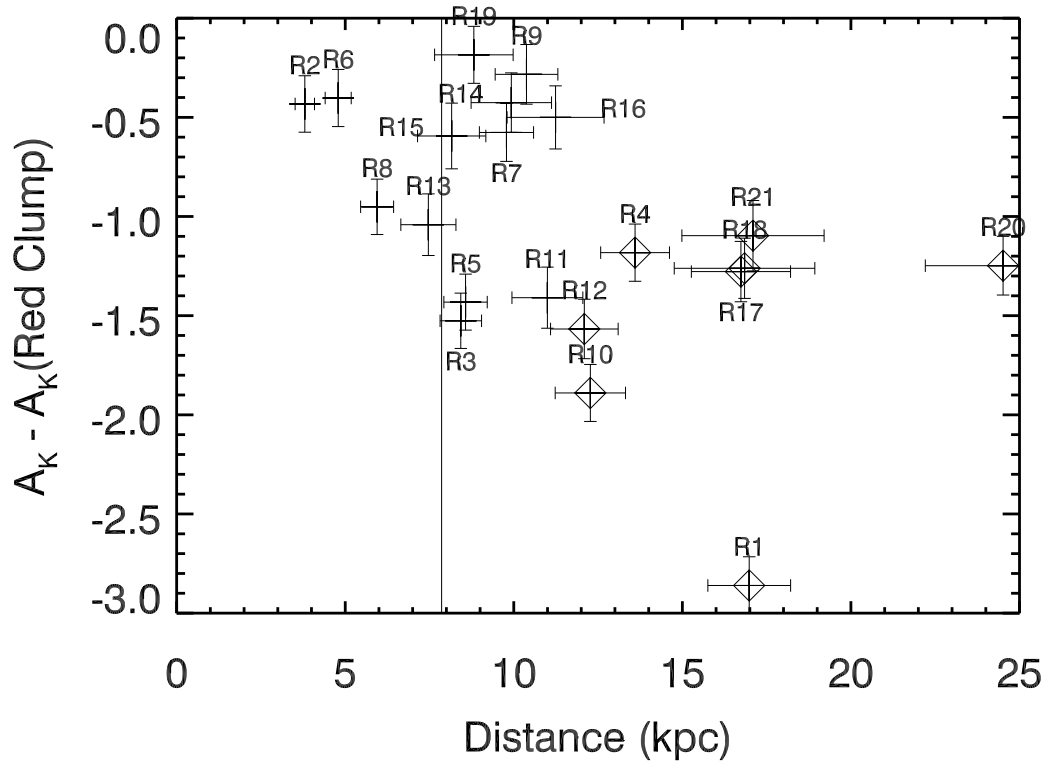


Fig. 6.— The distances derived in §2.3 vs the differences between the A_K derived in §2.3 and those from the extinction map given in Noguerras-Lara et al. (in preparation). The diamonds represent potential eclipsing binaries due to their large distances. The vertical line marks the location of the MWNSC (Boehle et al. 2016).

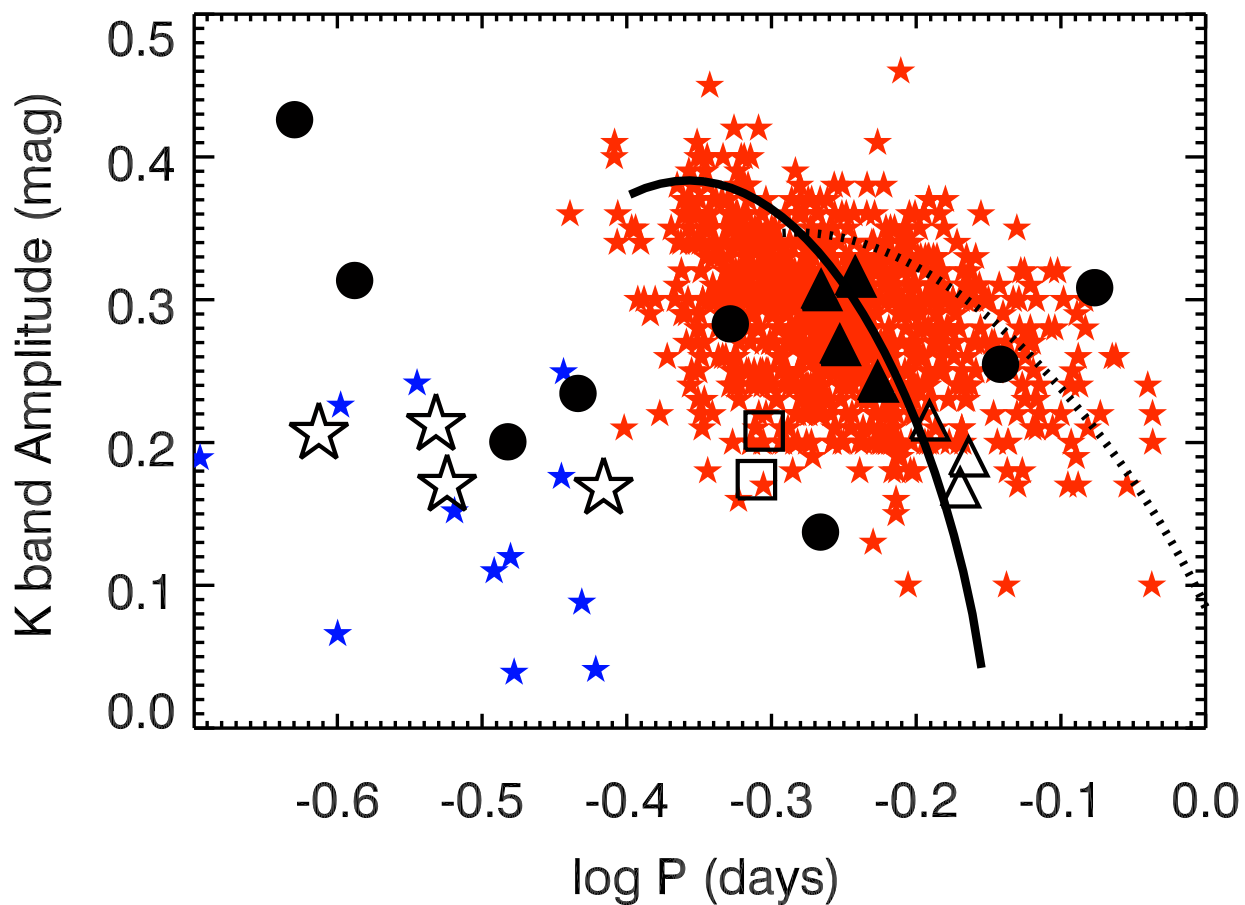


Fig. 7.— Bailey Diagram: K-band amplitude plotted against the logarithm of the period (d) of RRL stars. The small red and blue stars represent the RRab and RRc stars detected in the Galactic Bulge by the VVV survey (Gran et al. 2015, 2016). The large symbols are our variable stars with periods between 0.2 and 1 d: Stars for RRc candidates, filled triangles for identified RRab stars, open triangles for RRab candidates, filled circles for identified eclipsing binary candidates, and two open boxes for stars that may be RRab or eclipsing binaries. The black solid and dashed lines are the OoI and Oo II lines from Navarrete et al. (2015).

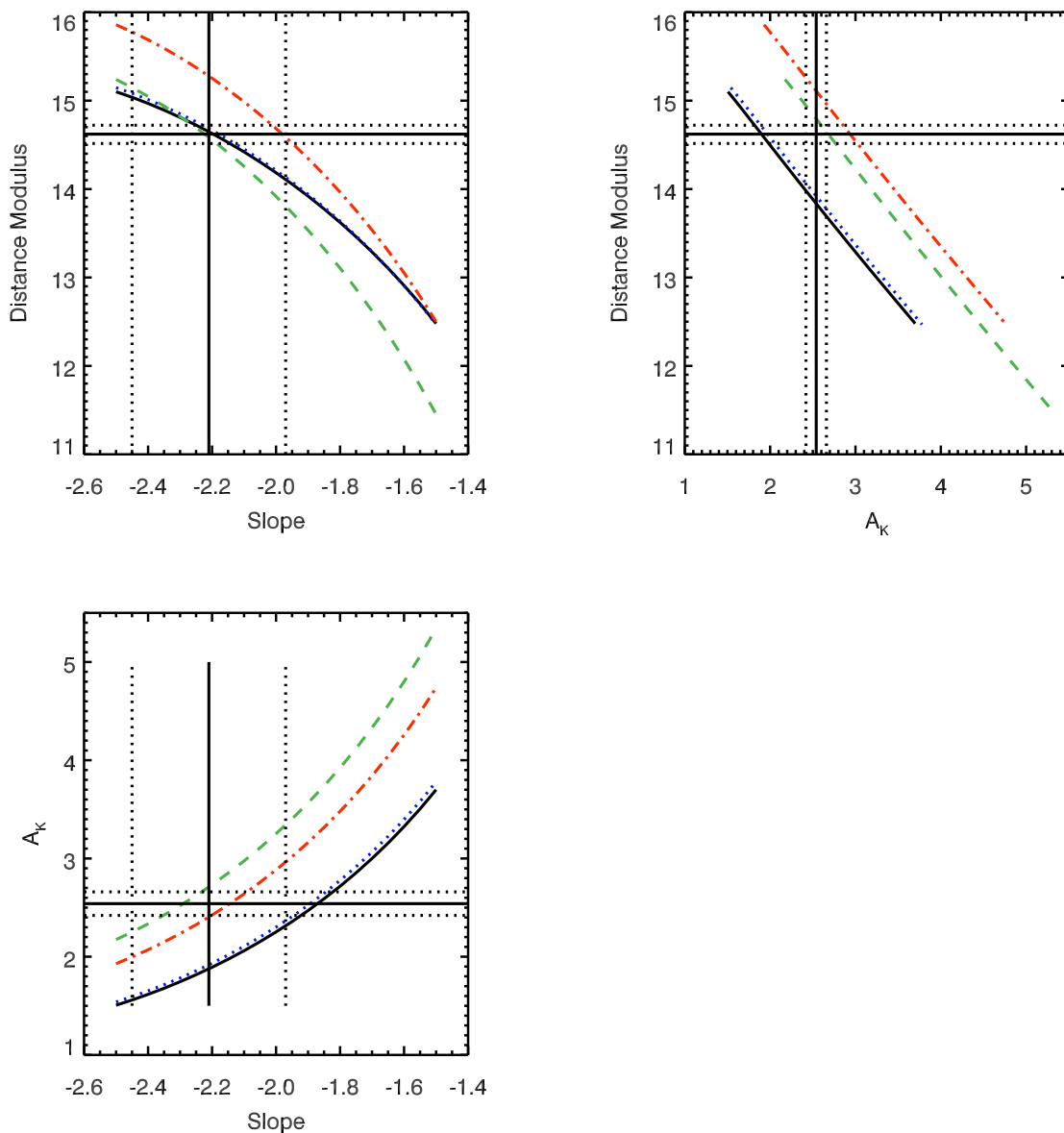


Fig. 8.— The correlation between distance modulus, absolute extinction A_{K_s} and the slope of the extinction law (α) for four candidate RRab stars (R3: black solid curve, R5: blue dotted curve, R15: green dashed curve, R16: red dot-dashed curve.) The horizontal and vertical solid and dashed lines in the three panels are the mean and 1 sigma uncertainty of the distance modulus, A_{K_s} and α of MWNSC given in Boehle et al. (2016) and Schödel et al. (2010).

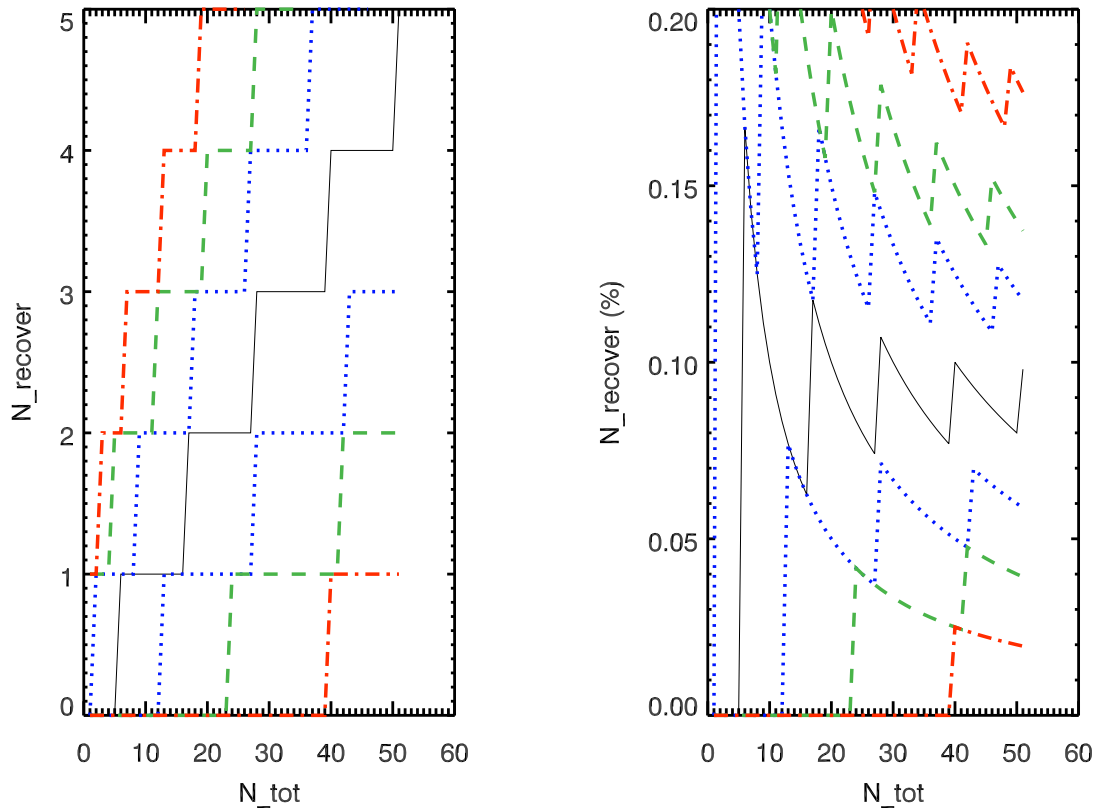


Fig. 9.— The recovered number (left) and fraction (right) of simulated RRab stars in the MWNSC. The black solid, blue dotted, green dashed and red dot-dashed lines represent the median, 68%, 90% and 99% percentile.

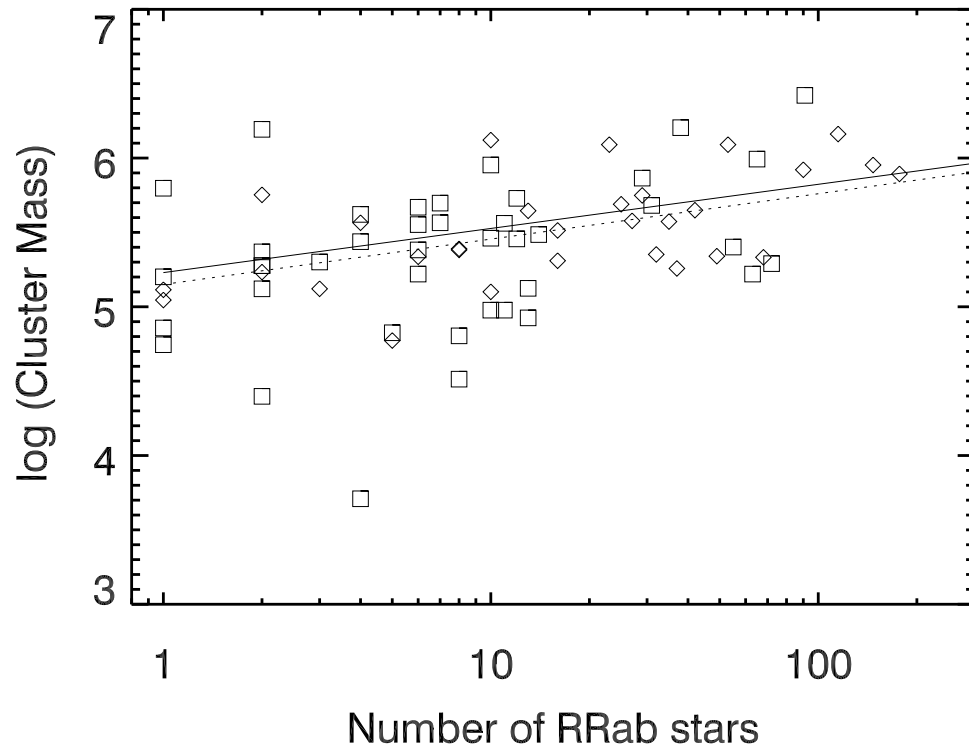


Fig. 10.— The relationship between the number of RRab stars and the logarithm of cluster mass in units of solar mass for the OoI (diamonds) and OoII (squares) clusters. The solid (OoI) and dashed (OoII) lines represents the Eqns. 11 and 12, respectively.

Table 3. Properties of probable RR Lyrae stars

| Name | M_{F127M} | M_{F153M} | M_{F127M} - | | Slope=-2.2 | | Slope=-2.1 | | Slope=-2.0 | |
|------|-------------|-------------|---------------|-------------|--|--|--|--|--|--|
| | | | M_{F153M} | $A_{K_s}^a$ | $A_{K_s}^a$ | Distance ^b | $A_{K_s}^a$ | Distance ^b | $A_{K_s}^a$ | Distance ^b |
| R1 | -0.24±0.05 | -0.39±0.04 | 0.15±0.01 | 3.27 | 0.40 ^{+0.10} _{-0.14} | 17.0 ^{+1.80} _{-1.31} | 0.44 ^{+0.11} _{-0.16} | 16.6 ^{+1.86} _{-1.36} | 0.48 ^{+0.12} _{-0.17} | 16.3 ^{+1.94} _{-1.41} |
| R2 | 0.24±0.05 | 0.19±0.04 | 0.04±0.01 | 2.85 | 2.41 ^{+0.10} _{-0.14} | 3.8 ^{+0.44} _{-0.33} | 2.63 ^{+0.11} _{-0.15} | 3.4 ^{+0.41} _{-0.30} | 2.87 ^{+0.12} _{-0.17} | 2.9 ^{+0.37} _{-0.28} |
| R3 | -0.27±0.05 | -0.42±0.04 | 0.15±0.01 | 3.42 | 1.89 ^{+0.10} _{-0.14} | 8.4 ^{+0.92} _{-0.68} | 2.06 ^{+0.11} _{-0.15} | 7.7 ^{+0.88} _{-0.65} | 2.25 ^{+0.12} _{-0.17} | 6.9 ^{+0.83} _{-0.61} |
| R4 | -0.60±0.05 | -0.82±0.04 | 0.23±0.01 | 2.77 | 1.59 ^{+0.10} _{-0.14} | 13.6 ^{+1.57} _{-1.19} | 1.73 ^{+0.11} _{-0.16} | 12.5 ^{+1.52} _{-1.14} | 1.89 ^{+0.12} _{-0.17} | 11.5 ^{+1.46} _{-1.09} |
| R5 | -0.24±0.05 | -0.39±0.04 | 0.15±0.01 | 3.37 | 1.93 ^{+0.10} _{-0.14} | 8.6 ^{+0.97} _{-0.72} | 2.11 ^{+0.11} _{-0.15} | 7.8 ^{+0.92} _{-0.69} | 2.30 ^{+0.12} _{-0.17} | 7.0 ^{+0.87} _{-0.64} |
| R6 | -0.16±0.05 | -0.29±0.04 | 0.13±0.01 | 3.00 | 2.59 ^{+0.10} _{-0.14} | 4.8 ^{+0.60} _{-0.46} | 2.83 ^{+0.11} _{-0.16} | 4.2 ^{+0.55} _{-0.41} | 3.09 ^{+0.12} _{-0.17} | 3.6 ^{+0.49} _{-0.37} |
| R7 | -0.43±0.05 | -0.62±0.04 | 0.19±0.01 | 2.73 | 2.15 ^{+0.10} _{-0.15} | 9.8 ^{+1.21} _{-0.90} | 2.34 ^{+0.11} _{-0.16} | 8.8 ^{+1.13} _{-0.84} | 2.56 ^{+0.12} _{-0.17} | 7.8 ^{+1.05} _{-0.77} |
| R8 | 0.04±0.05 | -0.05±0.04 | 0.09±0.01 | 3.34 | 2.39 ^{+0.10} _{-0.14} | 5.9 ^{+0.74} _{-0.56} | 2.61 ^{+0.11} _{-0.15} | 5.3 ^{+0.68} _{-0.51} | 2.85 ^{+0.12} _{-0.17} | 4.6 ^{+0.62} _{-0.46} |
| R9 | -0.42±0.05 | -0.61±0.04 | 0.19±0.01 | 2.42 | 2.13 ^{+0.11} _{-0.15} | 10.4 ^{+1.40} _{-1.05} | 2.32 ^{+0.12} _{-0.16} | 9.3 ^{+1.31} _{-0.97} | 2.54 ^{+0.13} _{-0.18} | 8.2 ^{+1.21} _{-0.90} |
| R10 | 0.16±0.05 | 0.10±0.04 | 0.06±0.01 | 3.54 | 1.65 ^{+0.10} _{-0.14} | 12.3 ^{+1.56} _{-1.16} | 1.79 ^{+0.11} _{-0.16} | 11.3 ^{+1.50} _{-1.11} | 1.96 ^{+0.12} _{-0.17} | 10.3 ^{+1.42} _{-1.05} |
| R11 | 0.25±0.05 | 0.21±0.04 | 0.04±0.01 | 3.35 | 1.94 ^{+0.11} _{-0.15} | 11.0 ^{+1.58} _{-1.18} | 2.11 ^{+0.12} _{-0.17} | 10.0 ^{+1.49} _{-1.11} | 2.31 ^{+0.13} _{-0.18} | 8.9 ^{+1.38} _{-1.03} |
| R12 | 0.07±0.05 | -0.01±0.04 | 0.08±0.01 | 3.61 | 2.05 ^{+0.11} _{-0.15} | 12.1 ^{+1.54} _{-1.17} | 2.23 ^{+0.12} _{-0.16} | 10.9 ^{+1.45} _{-1.09} | 2.44 ^{+0.13} _{-0.18} | 9.7 ^{+1.35} _{-1.01} |
| R13 | 0.40±0.05 | 0.40±0.04 | 0.01±0.01 | 3.38 | 2.34 ^{+0.11} _{-0.16} | 7.5 ^{+1.21} _{-0.89} | 2.55 ^{+0.12} _{-0.17} | 6.6 ^{+1.10} _{-0.81} | 2.79 ^{+0.13} _{-0.18} | 5.8 ^{+1.00} _{-0.73} |
| R14 | -0.17±0.05 | -0.30±0.04 | 0.13±0.01 | 2.86 | 2.43 ^{+0.11} _{-0.15} | 9.9 ^{+1.73} _{-1.26} | 2.65 ^{+0.12} _{-0.16} | 8.8 ^{+1.57} _{-1.13} | 2.89 ^{+0.13} _{-0.18} | 7.6 ^{+1.40} _{-1.01} |
| R15 | -0.32±0.05 | -0.48±0.04 | 0.16±0.01 | 3.33 | 2.73 ^{+0.12} _{-0.17} | 8.2 ^{+1.46} _{-1.05} | 2.98 ^{+0.13} _{-0.18} | 7.1 ^{+1.30} _{-0.94} | 3.25 ^{+0.14} _{-0.20} | 6.1 ^{+1.15} _{-0.83} |
| R16 | -0.29±0.05 | -0.45±0.04 | 0.16±0.01 | 2.92 | 2.42 ^{+0.11} _{-0.16} | 11.2 ^{+2.04} _{-1.45} | 2.64 ^{+0.12} _{-0.17} | 9.9 ^{+1.85} _{-1.31} | 2.88 ^{+0.13} _{-0.19} | 8.7 ^{+1.66} _{-1.17} |
| R17 | -0.13±0.05 | -0.25±0.04 | 0.12±0.01 | 3.24 | 1.97 ^{+0.11} _{-0.15} | 16.7 ^{+2.30} _{-1.77} | 2.14 ^{+0.12} _{-0.17} | 15.1 ^{+2.17} _{-1.66} | 2.34 ^{+0.13} _{-0.18} | 13.5 ^{+2.02} _{-1.54} |
| R18 | 0.36±0.05 | 0.34±0.04 | 0.02±0.01 | 3.13 | 1.87 ^{+0.11} _{-0.15} | 16.8 ^{+3.04} _{-2.21} | 2.04 ^{+0.12} _{-0.17} | 15.3 ^{+2.83} _{-2.05} | 2.22 ^{+0.13} _{-0.18} | 13.8 ^{+2.61} _{-1.89} |
| R19 | -0.38±0.05 | -0.56±0.04 | 0.18±0.01 | 3.22 | 3.03 ^{+0.10} _{-0.14} | 8.8 ^{+1.67} _{-1.20} | 3.30 ^{+0.16} _{-0.16} | 7.6 ^{+1.46} _{-1.05} | 3.61 ^{+0.12} _{-0.17} | 6.4 ^{+1.25} _{-0.90} |
| R20 | -0.48±0.05 | -0.67±0.04 | 0.20±0.01 | 3.29 | 2.04 ^{+0.10} _{-0.15} | 24.5 ^{+3.72} _{-2.92} | 2.22 ^{+0.11} _{-0.16} | 22.1 ^{+3.46} _{-2.70} | 2.43 ^{+0.12} _{-0.18} | 19.7 ^{+3.18} _{-2.47} |
| R21 | 0.43±0.05 | 0.43±0.04 | 0.00±0.01 | 3.15 | 2.05 ^{+0.13} _{-0.18} | 17.1 ^{+3.28} _{-2.51} | 2.24 ^{+0.14} _{-0.19} | 15.4 ^{+3.03} _{-2.31} | 2.44 ^{+0.15} _{-0.21} | 13.7 ^{+2.78} _{-2.11} |

Note. — ^a, in units of mag; ^b, in units of kpc